Analysis of the small-angle neutron scattering of nanocrystalline ferromagnets using a micromagnetics model

J. Weissmüller
Forschungszentrum Karlsruhe, Institut für Nanotechnologie, Karlsruhe, Germany and Universität des Saarlandes, Technische Physik, Saarbrücken, Germany

A. Michels
Universität des Saarlandes, Technische Physik, Saarbrücken, Germany

J. G. Barker
National Institute of Standards and Technology, NCNR, Gaithersburg, Maryland 20899

A. Wiedenmann
Hahn-Meitner-Institut, BENSC, Berlin, Germany

U. Erb
Department of Metallurgy, University of Toronto, Toronto, Canada

R. D. Shull
National Institute of Standards and Technology, MSEL, Gaithersburg, Maryland 20899
(Received 9 November 2000; published 10 May 2001)

In ferromagnets with a nonuniform magnetocrystalline and/or magnetoelastic anisotropy, such as nanocrystalline (nc-) or cold-worked (cw-) polycrystalline materials, the static magnetic microstructure gives rise to strong elastic magnetic small-angle neutron scattering (SANS). The paper explores a method for analyzing field-dependent SANS data from such materials in terms of a model based on the theory of micromagnetics. Samples of cw Ni and of electrodeposited nc Ni and nc Co were characterized by x-ray scattering and magnetometry, and were investigated by SANS both with and without polarization of the neutron beam. The variation of the differential scattering cross section with the scattering vector and with the applied magnetic field is well described by the model. Also, experimental results for the exchange stiffness constant A and for the spin-wave stiffness constant D obtained from the analysis are found to agree with literature data obtained by inelastic neutron scattering on single-crystal specimens. The model supplies an ''anisotropy field scattering function'' that contains information on the magnitude of the magnetic anisotropy in the material, and on the characteristic length scales on which the anisotropy changes direction. The results suggest that the anisotropy may be strongly nonuniform in each crystallite, possibly due to twinning, and that some magnetic moments in the Ni samples are strongly pinned at defects.

DOI: 10.1103/PhysRevB.63.214414 PACS number(s): 75.50.Kj, 61.12.Ex, 81.07.−b, 75.30.Ds

I. INTRODUCTION

The favorable magnetic properties of nanocrystalline ferromagnets have led to a number of applications both as hard and as soft magnetic materials. Essentially, the reduction of the grain size d to the nanometer scale influences the magnetic properties by introducing random jumps in the orientation of the magnetic ''easy axes'' on the scale of nanometers. It has been shown that the effect of the reduced grain size on the magnetic properties depends critically on the magnitude of the grain size relative to a magnetic exchange length $l_K = \sqrt{A/K}$ with A the ferromagnetic exchange-stiffness constant and K an anisotropy energy coefficient. Nanocrystalline hard magnets have $l_K < d$ with the magnetization locked into the easy axes of each grain and an enhanced remanence due to gradients in the orientation of the magnetization at grain boundaries.[1,2] By contrast, nanocrystalline soft magnets have $l_K > d$; in this case the magnetization cannot follow the changes in the orientation of the easy axes on the scale of the grain size. Instead, the magnetization probes an effective average of the anisotropy in many neighboring grains the magnitude of which drops steeply with decreasing size.[3] Obviously, it is of interest to have at ones disposal the techniques for measuring the relevant length scales, or the quantities that determine them, in nanocrystalline ferromagnets.

The grain size is routinely measured, e.g., by diffraction or transmission electron microscopy, but the length scale of relevance for the magnetic properties would appear to be a mean distance between changes in the direction of the anisotropy. Since lattice defects and strain fields will also influence this quantity, the grain size may not always be an adequate parameter to describe the relation between the microstructure and the magnetic properties. While the anisotropy energy coefficients are known for single crystals and summary information on the magnetic anisotropy can be obtained by analysis of the approach to saturation in a magnetization isotherm,[4] there are no known techniques for characterizing the microstructure of the anisotropy field in dense nanocrystalline materials.

Similarly, few data are available for the ferromagnetic exchange-stiffness constant in nanocrystalline solids, and, in particular, there are no measurements of A in single-component nanocrystalline ferromagnets, which constitute simple model systems for ferromagnetism in nanocrystalline materials. A is defined so that the exchange energy density in gradients of the magnetization is $A|\nabla v|^2$ with v a unit vector in the direction of the magnetization (see Ref. 5 and Sec. 16.1 in Ref. 6); besides determining l_K, A is an important material parameter in the theory of micromagnetics, a continuum approach that deals with the variation of the direction of the magnetization as a function of position and time.[7,8] Among the phenomena that are described by micromagnetics are domain walls,[9] spin waves,[5] the effect of lattice defects on the approach to saturation,[4] the so-called ''magnetization ripple'' in thin films,[10,11] and the magnetic properties of amorphous ferromagnets.[12] More recently, several analytical and numeric treatments of the magnetic microstructure and of macroscopic magnetic properties of nanocrystalline hard and soft magnets, based on the micromagnetics theory, have been proposed.[13,14]

Small-angle neutron scattering (SANS) experiments can supply information on the magnetic microstructure in the bulk of nanocrystalline materials with a resolution that covers length scales in the nanometer regime. Several SANS studies have investigated ferromagnetic nanoparticles isolated by a nonmagnetic matrix where the magnetic interaction between neighboring particles is weak or negligible.[15–17] By contrast, adjacent grains in bulk nanocrystalline ferromagnets, that are the subject of the present work, are strongly coupled via the exchange interaction at grain boundaries; indeed, SANS data indicate that the local orientation of the magnetization can be correlated over many neighboring grains.[18,19] This is well supported by micromagnetics theory,[3] and suggests that micromagnetics and magnetic SANS theory may be combined to provide a quantitative analysis of experimental SANS data. In the past, this approach has been applied successfully to the study of cold-worked ferromagnetic single crystals, where it provided information on the dislocation arrangement.[20] However, for lack of a more adequate theory, SANS data of bulk nanocrystalline ferromagnets were generally analyzed in terms of scattering by sets of hard spheres with a distribution of sizes,[18,19,21] a model adopted from nuclear scattering without rigorous examination of its applicability to magnetic scattering by nanocrystalline ferromagnets. Recently, quite general results for the dependency of the differential scattering cross-section of ferromagnets with a nonuniform magnetic anisotropy on the magnetic field and on the scattering vector have been derived from the theory of micromagnetics.[22] It was suggested that analyzing experimental SANS data of nanocrystalline ferromagnets in terms of the theory may provide quantitative information on (i) the magnetic microstructure, (ii) the exchange stiffness constant and (iii) the magnitude and microstructure of the magnetic anisotropy. The purpose of the present work is to check the theory against experimental data and to explore how far meaningful information can be obtained. Preliminary results of this study have been communicated in Ref. 23.

The nanocrystalline samples under investigation are elemental Ni and Co of high purity and mass density prepared by pulsed electrodeposition.[24,25] Compared to the previously studied elemental nanocrystalline materials prepared by inert-gas condensation[18,19] and to multiphase nanocrystalline ferromagnets crystallized from the glass,[21] our samples have much smaller nuclear scattering contrast from pores or second phases, or, in other words, a considerably more favorable ratio of (magnetic) scattering signal to (nuclear) background.

The paper is organized as follows: Section II discusses the theory of magnetic SANS of nanocrystalline ferromagnets; in the interest of a self-contained presentation, Secs. II A and II B summarize, respectively, the relevant elements of the well-known formalisms of micromagnetics and of magnetic SANS. Section II C shows how the results are combined to derive the expressions for the field dependence of the differential scattering cross section that are the focus of attention of this paper. For conciseness, we summarize only the derivation for isotropic materials in the main text; the Appendix presents the generalization to anisotropic microstructures and shows that the effects of texture on the results are small. Finally, Sec. II D discusses how the theory can be combined with experimental data to measure the ferromagnetic exchange-stiffness constant and the anisotropy field-scattering function introduced in Sec. II C. This requires separating SANS by the magnetic microstructure from SANS due to variation in the atomic density or to second phases; we discuss how the separation can be achieved, alternatively, by analysis of the dependence of SANS on the magnetic field using nonpolarized neutrons, or by varying the polarization of the incident neutron beam at constant field. Section III describes the experiment and data reduction, followed by the presentation of the results for the nuclear microstructure and for the magnetic properties by wide-angle x-ray scattering and magnetometry, respectively, and of the SANS data in Sec. IV. Sections V and VI present discussion and conclusions, respectively.

II. THEORY

A. Micromagnetics

We intend to model the static magnetic microstructure, that is, the spatial variation of the orientation of the magnetization vector at equilibrium, in dense, single-phase materials with a highly nonuniform magnetocrystalline and/or magnetoelastic anisotropy; examples for such materials are nanocrystalline or cold-worked single crystalline or polycrystalline materials. With this in mind, we consider a material with uniform values of the atomic density ρ_a, atomic magnetic moment μ_a, and exchange-stiffness constant A, but with a nonuniform magnetic anisotropy. More precisely, we allow the anisotropy energy density a to depend not only on the magnetization $\mathbf{M}(\mathbf{x})$ but also explicitly on the position $\mathbf{x}$. An *anisotropy field* (or perturbing field) $\mathbf{H}_P$ is defined as the derivative of a with respect to the orientation of the magnetization. In SI units, with $\mathbf{v}$ a unit vector along $\mathbf{M}$, $\mathbf{v}=\mathbf{M}/M_S$ where M_S denotes the saturation magnetization $M_S=\rho_a\mu_a$,

$$\mathbf{H_P} = -\frac{1}{\mu_0 M_S}\frac{\partial a}{\partial \mathbf{v}}. \quad (1)$$

By definition, the vector $\mathbf{H}_P$ is normal to $\mathbf{M}$ and acts as a torque on $\mathbf{M}$; like a, $\mathbf{H}_P$ varies as a function of $\mathbf{x}$ and of $\mathbf{M}$. Below, we shall introduce the restrictive assumption that the material be nearly saturated, so that the magnetization is nearly aligned with the direction of the applied magnetic field and only small variations of $\mathbf{M}$ about this direction are of interest. It is then permitted to neglect the dependency of $\mathbf{H}_P$ on $\mathbf{M}$, and retain only $\mathbf{H}_P = \mathbf{H}_P(\mathbf{x})$, with the understanding that $\mathbf{H}_P$ be computed for $\mathbf{M}$ parallel to the applied magnetic field. The grain size, crystallographic texture, and strain in the material enter our theory exclusively through the magnitude and spatial structure of $\mathbf{H}_P$ near saturation, that is, through the ''anisotropy field microstructure.'' For instance, in an idealized nanocrystalline material, each grain has its individual, uniform magnitude and orientation of $\mathbf{H}_P$.

At static equilibrium, the torques on the magnetization due to (i) the exchange interaction, (ii) the magnetic field $\mathbf{H}$, and (iii) the anisotropy field must be balanced; this requires that[26]

$$\left(\frac{2A}{\mu_0 M_S^2}\{\nabla^2 M_x, \nabla^2 M_y, \nabla^2 M_z\} + \mathbf{H}(\mathbf{x}) + \mathbf{H}_p(\mathbf{x})\right) \times \mathbf{M}(\mathbf{x}) = 0. \quad (2)$$

The magnetic field $\mathbf{H}$ is the sum of the applied field $\mathbf{H}_a$ and of the demagnetizing field $\mathbf{H}_d$, which can be separated into two components: the field $\mathbf{H}_d^s$, which arises from the discontinuity of $\mathbf{M}$ at the macroscopic sample surface, and the field $\mathbf{H}_d^b(\mathbf{x})$, which arises from the divergence of $\mathbf{M}(\mathbf{x})$ in the bulk. $\mathbf{H}_d^s$ varies slowly with position in the material and is approximated by the uniform field $\mathbf{H}_d^s = -N_d\langle\mathbf{M}\rangle$, with the demagnetizing factor N_d dependent on the sample geometry. $\langle\mathbf{M}\rangle$ denotes the macroscopic magnetization. Because of the uniformity of M_S and A, $\mathbf{M}$ is continuous at grain boundaries, therefore $\mathbf{H}_d^s$ is exclusively from the macroscopic external surface of the material, and is entirely unrelated to the size or shape of grains in the nanocrystalline material.

In the limit where the angle of misalignment of the magnetic moments relative to $\langle\mathbf{M}\rangle$ is small, Eq. (2) can be linearized[7] by neglecting terms that are of second order in $\mathbf{M}_P(\mathbf{x})$, the component of the magnetization perpendicular to the macroscopic magnetization; $\mathbf{M}_P(\mathbf{x}) = \mathbf{M}(\mathbf{x}) - \langle\mathbf{M}\rangle$. It has been shown[5,27] that, with the anisotropy field and the magnetization expressed in terms of their Fourier transforms,

$$\mathbf{H}_P(\mathbf{x}) = (2\pi)^{-3/2}\int\int\int_{-\infty}^{\infty}\mathbf{h}(\mathbf{q})\exp(-i\mathbf{q}\mathbf{x})d\mathbf{q}, \quad (3)$$

$$\mathbf{M}_P(x)/M_S = (2\pi)^{-3/2}\int\int\int_{-\infty}^{\infty}\mathbf{m}(\mathbf{q})\exp(-i\mathbf{q}\mathbf{x})d\mathbf{q}, \quad (4)$$

the linearized equation can be solved independently for each wave vector $\mathbf{q}$. Analytical solutions to Eq. (2) have been considered in various contexts, generally assuming specific functional dependencies of a or of $\mathbf{H}_P$ on $\mathbf{M}$ and on $\mathbf{x}$; this includes amorphous ferromagnets with random anisotropy (ignoring $\mathbf{H}_d^b$),[12] thin films,[11,28] and cubic single crystals with $\mathbf{H}_P(\mathbf{x})$ due to magnetostriction, for instance, in the strain field of a dislocation.[4] For an arbitrary dependency of $\mathbf{H}_P$ on $\mathbf{x}$, the solution in the limit of small misalignment is[22]

$$\mathbf{m}(\mathbf{q}) = \frac{\mathbf{h}(\mathbf{q})}{H_{\rm eff} + M_S\sin^2\vartheta} + \frac{M_S}{H_{\rm eff}}\frac{\mathbf{q}_\perp \times [\mathbf{h}(\mathbf{q}) \times \mathbf{q}_\perp]}{q^2(H_{\rm eff} + M_S\sin^2\vartheta)}. \quad (5)$$

The vector $\mathbf{q}_\perp$ denotes the component of $\mathbf{q}$ that is normal to the applied field $\mathbf{H}_a$, and ϑ is the angle between $\mathbf{q}$ and $\mathbf{H}_a$, see Fig. 1. $H_{\rm eff}$ denotes an *effective magnetic field*, defined by

$$H_{\rm eff}(q, H_i) = H_i[1 + l_H^2(H_i)q^2]. \quad (6)$$

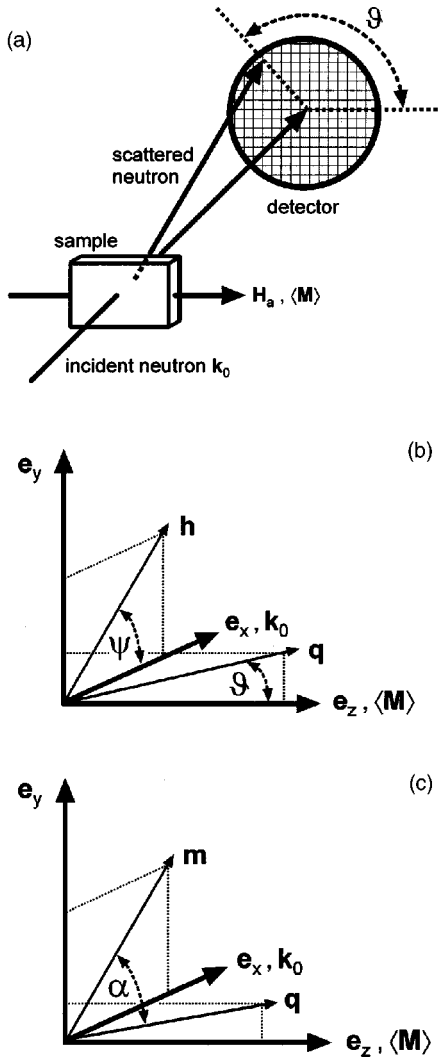

FIG. 1. Illustration of the scattering geometry (a) and of the angles ϑ, ψ, and α [(b) and (c)]. The Fourier coefficients $\mathbf{h}$ and $\mathbf{m}$ of the anisotropy field and of the reduced magnetization, respectively, are confined to the plane normal to the mean magnetization $\langle\mathbf{M}\rangle$ and the scattering vector $\mathbf{q}$ is normal to the incident neutron wave vector, $\mathbf{k}_0$. The symbols $\mathbf{e}_x$, $\mathbf{e}_y$, $\mathbf{e}_z$ denote the unit vectors along the coordinate axes.

$H_{\rm eff}$ depends on the magnitude of the *internal field* $\mathbf{H}_i = \mathbf{H}_a + \mathbf{H}_d^s$ and on the *exchange length of the internal field* l_H,[4] defined by

$$l_H = \left(\frac{2A}{\mu_0 M_S H_i} \right)^{1/2}. \tag{7}$$

By inspection of Eq. (5) it is seen that the effect of the effective magnetic field is to suppress the fluctuations of the magnetization. Equation (6) may, alternatively, be expressed as $H_{\rm eff} = H_i + M_S l_M^2 q^2$, where l_M denotes the magnetostatic exchange length[4] $l_M = \sqrt{2A/(\mu_0 M_S^2)}$; it is then readily seen that $H_{\rm eff}$ approximates the internal field at small q, whereas $H_{\rm eff}$ at high q is dominated by the term $M_S l_M^2 q^2$, which is related to the exchange interaction and the stray field, but is independent of the applied field. Increasing the applied magnetic field will therefore result in a relatively larger increase of $H_{\rm eff}$ at smaller q, thereby suppressing selectively those fluctuations of the magnetization with the longest wavelength. As a consequence, the dominant wavelength of the magnetic fluctuations will evolve to ever smaller values as the magnetic field is increased.

It is also instructive to consider Eq. (5) in the limit $H_{\rm eff} \gg M_S$, where $\mathbf{m}(\mathbf{q}) \approx \mathbf{h}(\mathbf{q})/H_{\rm eff}$. Because of the convolution theorem, the product in reciprocal space corresponds in real space to the convolution with the Fourier transform of $1/H_{\rm eff}$, which is a decaying exponential with a characteristic length l_H. In other words, the magnetic microstructure is the convolution of the anisotropy field microstructure with an exponential response function with a characteristic length l_H that varies as the reciprocal root of the internal field. At small applied magnetic fields l_H may be larger than the grain size; in this case the anisotropy fields of the individual grains in a nanocrystalline ferromagnet are decorated by static fluctuations of the magnetization that extend over several neighboring grains, so that the individual fluctuations can strongly overlap.

B. Small-angle neutron scattering

Magnetic neutron scattering is the subject of several monographs, for instance, Refs. 29–32. Our discussion of magnetic SANS, both with and without polarization of the incident beam, is based on the results in Ref. 33. For elastic scattering, and neglecting spin-dependent nuclear scattering, the differential scattering cross sections at scattering vector $\mathbf{q}$ due to atoms at positions $\mathbf{x}_j$, obey (see also Sec. 2.3.3 in Ref. 32)

$$\frac{d\Sigma^{\pm\pm}}{d\Omega}(\mathbf{q}) = \frac{1}{V} \sum_{j,l} \exp[i\mathbf{q}(\mathbf{x}_j - \mathbf{x}_l)] \times (b_{{\rm nuc},j} b_{{\rm nuc},l} \pm b_{{\rm nuc},j} b_{{\rm mag},l} Q_{l,z} \pm b_{{\rm nuc},l} b_{{\rm mag},j} Q_{j,z} + b_{{\rm mag},j} b_{{\rm mag},l} Q_{j,z} Q_{l,z}), \tag{8}$$

$$\frac{d\Sigma^{\pm\mp}}{d\Omega}(\mathbf{q}) = \frac{1}{V} \sum_{j,l} \exp[i\mathbf{q}(\mathbf{x}_j - \mathbf{x}_l)] b_{{\rm mag},j} b_{{\rm mag},l} \times [Q_{j,x} Q_{l,x} + Q_{j,y} Q_{l,y} \mp i\mathbf{e}_z \cdot (\mathbf{Q}_j \times \mathbf{Q}_l)], \tag{9}$$

where $b_{\rm nuc}$ and $b_{\rm mag}$ denote the atomic nuclear and magnetic scattering lengths, respectively, and $\mathbf{Q}$ represents the Halpern-Johnson vector, which is related to a unit vector $\boldsymbol{\varepsilon}$ in the direction of $\mathbf{q}$ and to the atomic magnetic moment $\boldsymbol{\mu}_a$ by the vector function $\mathbf{Q} = \boldsymbol{\varepsilon}(\boldsymbol{\varepsilon} \cdot \boldsymbol{\mu}_a/\mu_a) - \boldsymbol{\mu}_a/\mu_a$.[34,35] The superscripts to $d\Sigma/d\Omega$ denote the spin states of the incident and of the scattered neutron, e.g., $d\Sigma^{+-}/d\Omega$ ($d\Sigma^{++}/d\Omega$) relates to ''spin-flip'' (''spin-non-flip'') scattering with the incident and scattered spin in the + and − (+ and +) directions, respectively, relative to the unit vector $\mathbf{e}_z$. The latter is parallel to the magnetic field and defines the direction of quantization of the neutron spin.

Equations (8) and (9) account for scattering due to variations in the atomic density and composition and to variations in the magnitude and orientation of the magnetic moment. Our discussion of micromagnetics in Sec. II A assumes an ideal material with uniform density and composition; the scattering cross section would then be exclusively due to the variation in the spin orientation. However, in real samples the atomic density and the magnitude of the moment will not be perfectly uniform, for instance, due to missing atoms and missing moments in pores. We assume such nuclear defects to be uncorrelated to the variations of the anisotropy field that gives rise to the magnetic microstructure discussed above and to the magnetic scattering that is of interest here; there is then no interference between the respective scattering amplitudes, and the combined nuclear and magnetic ''residual'' scattering cross section $d\Sigma_R/d\Omega$ due to the nonuniform density and composition is additive to the scattering cross section of the spin misalignment $d\Sigma_M/d\Omega$. In order to separate the two contributions formally, we decompose the vectors $\boldsymbol{\mu}_{a,j}$ into the value for the perfectly aligned state, $\hat{\boldsymbol{\mu}}_{a,j} = \mu_{a,j}\mathbf{e}_z$ and the difference vector $\Delta\boldsymbol{\mu}_{a,j} = \boldsymbol{\mu}_{a,j} - \hat{\boldsymbol{\mu}}_{a,j}$. The vectors $\mathbf{Q}_j$ are decomposed analogously, $\hat{\mathbf{Q}} = \boldsymbol{\varepsilon}(\boldsymbol{\varepsilon} \cdot \mathbf{e}_z) - \mathbf{e}_z$ and $\mathbf{Q}_j = \hat{\mathbf{Q}} + \Delta\mathbf{Q}_j$, and the latter expression is substituted into Eqs. (8) and (9). Attention is restricted to small misalignment of the moments and to situations where the mean magnetization is along the direction of quantization $\mathbf{e}_z$; the $\Delta\boldsymbol{\mu}_{a,j}$ are then normal to $\mathbf{e}_z$ and their mean value vanishes. Since $\mathbf{Q}$ is a linear vector function of $\boldsymbol{\mu}_a$ the mean value of $\Delta\mathbf{Q}$ will also vanish. When there is no interference between the spin misalignment and variation of the nuclear density then the contributions of terms containing $b_{{\rm nuc},j}\, b_{{\rm mag},l}\, \Delta\mathbf{Q}_l$ or $b_{{\rm mag},j}\, b_{{\rm mag},l}\, \hat{\mathbf{Q}}\Delta\mathbf{Q}_l$ to the sums in Eqs. (8) and (9) will cancel. The remaining terms can be grouped into the two additive scattering cross sections $d\Sigma_R/d\Omega$ and $d\Sigma_M/d\Omega$, the first containing only terms $b_{\rm nuc}$ and $b_{\rm mag}\hat{\mathbf{Q}}$, and the second only terms $b_{\rm mag}\Delta\mathbf{Q}$. In displaying the results we also combine terms with and without spin flip, e.g., $d\Sigma^{+}/d\Omega = d\Sigma^{++}/d\Omega + d\Sigma^{+-}/d\Omega$, to account for the fact that the SANS instrumentation that is of interest to the present work has no polarization analysis:

$$\frac{d\Sigma_R^{\pm}}{d\Omega}(\mathbf{q}) = \frac{1}{V}\sum_{j,l} \exp[i\mathbf{q}(\mathbf{x}_j - \mathbf{x}_l)] \times [b_{\mathrm{nuc},j} b_{\mathrm{nuc},l} + b_{\mathrm{mag},j} b_{\mathrm{mag},l} |\hat{\mathbf{Q}}|^2 \pm b_{\mathrm{nuc},j} b_{\mathrm{mag},l} \hat{Q}_z \pm b_{\mathrm{nuc},l} b_{\mathrm{mag},j} \hat{Q}_z], \tag{10}$$

$$\frac{d\Sigma_M^{\pm}}{d\Omega}(\mathbf{q}) = \frac{1}{V}\sum_{j,l} \exp[i\mathbf{q}(\mathbf{x}_j - \mathbf{x}_l)] b_{\mathrm{mag},j} b_{\mathrm{mag},l} [(\Delta\mathbf{Q}_j \cdot \Delta\mathbf{Q}_l) \mp i\mathbf{e}_z \cdot (\Delta\mathbf{Q}_j \times \Delta\mathbf{Q}_l)]. \tag{11}$$

In the simplest case, each of the scattering lengths b_{nuc} and b_{mag} has identical values at all sites. It is then readily seen that Eq. (10) reduces to the well-known expression for scattering by magnetically aligned systems, such as saturated ferromagnetic particles in a nonmagnetic matrix:[29]

$$\frac{d\Sigma_R^{\pm}}{d\Omega}(\mathbf{q}) = \frac{1}{V}(b_{\mathrm{nuc}}^2 \mp 2 b_{\mathrm{nuc}} b_{\mathrm{mag}} \sin^2\vartheta + b_{\mathrm{mag}}^2 \sin^2\vartheta) \times \sum_{j,l} \exp[i\mathbf{q}(\mathbf{x}_j - \mathbf{x}_l)]. \tag{12}$$

It can be seen that the interference between nuclear and magnetic scattering gives rise to a dependency of the residual scattering cross section on the polarization of the incident beam. In spite of the absence of interference between nuclear and magnetic scattering, Eq. (11) for the spin misalignment scattering also has a polarization-dependent term, involving the cross product $\mathbf{Q}_j \times \mathbf{Q}_l$. This term depends on the angle included by the pair of spins j, l and, unless the spins take a helical structure with a preferred direction of rotation, it will take either sign with equal probability, independent of the interatomic distance. Therefore, the cross product does not generally contribute to the sum in Eq. (11), and the spin-misalignment scattering will be independent of the polarization. By omitting the terms $\mathbf{Q}_j \times \mathbf{Q}_l$ we can write Eq. (11) in a form that is more suitable for combination with the results in Sec. II A:

$$\frac{d\Sigma_M}{d\Omega}(\mathbf{q}) = \frac{1}{V}\left|\sum_j b_{\mathrm{mag},j} \Delta\mathbf{Q}_j \exp(i\mathbf{q}\mathbf{x}_j)\right|^2. \tag{13}$$

For small-angle scattering the discreteness of the atomic structure of matter is of no importance, so that the sum in Eq. (13) can, quite analogously to the usual procedure in nuclear small-angle scattering, be replaced by an integral based on the continuous function, $\Delta\mathbf{Q}(\mathbf{x}) = \varepsilon[\varepsilon \cdot \mathbf{M}_P(\mathbf{x})/M_S] - \mathbf{M}_P(\mathbf{x})/M_S$. By comparing with Eq. (4) it is seen that the magnetic scattering cross section can then be expressed as

$$\frac{d\Sigma_M}{d\Omega}(\mathbf{q}) = \frac{8\pi^3}{V} b_{\mathrm{mag}}^2 \rho_a^2 |\mathbf{p}(\mathbf{q})|^2, \tag{14}$$

where $\mathbf{p}(\mathbf{q}) = \varepsilon[\varepsilon \cdot \mathbf{m}(\mathbf{q})] - \mathbf{m}(\mathbf{q})$ and $|\mathbf{p}(\mathbf{q})|^2 = |\mathbf{m}(\mathbf{q})|^2 \sin^2\alpha$, with α the angle included by $\mathbf{m}$ and $\mathbf{q}$ (see Fig. 1). Equation (14) is similar to previous results for the cross section for spin-only magnetic neutron scattering in terms of the Fourier transform of the magnetization (e.g., Ref. 30), but it expresses the scattering cross section in terms of the Fourier transform of $\mathbf{M}_P$ instead of $\mathbf{M}$.

C. SANS by the magnetic microstructure

We shall now investigate scattering by a magnetic microstructure that satisfies Eq. (5). In doing so, we restrict our attention to scattering geometries with the incident neutron beam normal to the direction of the applied field (more precisely, normal to $\langle\mathbf{M}\rangle$). We use Cartesian coordinates with $\langle\mathbf{M}\rangle$ along the unit vector $\mathbf{e}_z$ and with the incident neutron beam along $\mathbf{e}_x$ (see Fig. 1); the anisotropy field and, consequently, its Fourier components, are then in the plane containing $\mathbf{e}_x$ and $\mathbf{e}_y$, and the scattering vector is in the plane containing $\mathbf{e}_y$ and $\mathbf{e}_z$:

$$\mathbf{h} = h\{\cos\psi, \sin\psi, 0\}, \quad \mathbf{q} = q\{0, \sin\vartheta, \cos\vartheta\},$$

which defines the angle ψ.

Straightforward algebra shows that, when Eq. (5) is substituted for $\mathbf{m}(\mathbf{q})$ in Eq. (14) for the scattering cross section, the result can be written as

$$\frac{d\Sigma_M}{d\Omega}(\mathbf{q}, H_i) = S_H(\mathbf{q}) R(\psi, \vartheta, q, H_i), \tag{15}$$

$$S_H(\mathbf{q}) = \frac{8\pi^3}{V} b_{\mathrm{mag}}^2 \rho_a^2 \frac{h^2(\mathbf{q})}{M_S^2}, \tag{16}$$

$$R(\psi, \vartheta, q, H_i) = \frac{M_S^2}{H_{\mathrm{eff}}^2(q, H_i)} \cos^2\psi + \frac{M_S^2}{[H_{\mathrm{eff}}(q, H_i) + M_S \sin^2\vartheta]^2} \sin^2\psi \cos^2\vartheta. \tag{17}$$

Equations (15)–(17) imply that $d\Sigma_M/d\Omega$ can be expressed as the product of an *anisotropy-field scattering function* $S_H(\mathbf{q})$, that depends only on the microstructure of the anisotropy field, but not on the applied magnetic field, and of a dimensionless *micromagnetics response function for SANS*, $R(\psi, \vartheta, q, H_i)$, that depends on the applied field and on the scattering vector, but not on the geometry of the microstructure.

It is seen that the differential scattering cross section depends not only on the *magnitude* of the Fourier components $\mathbf{h}(\mathbf{q})$ of the anisotropy field, but also (through the angle ψ) on their *orientation*. Therefore, the variation of $d\Sigma_M/d\Omega$ with $\mathbf{H}$ and $\mathbf{q}$ may depend on the crystallographic texture and on other forms of anisotropy of the sample properties. For simplicity, we shall here consider the isotropic case, where $\mathbf{h}(\mathbf{q})$ take on all angles ψ with equal probability. In the Appendix, we examine the more general case of an arbitrary texture in the orientation of the anisotropy field, and show that the texture has only small effects on the results for the scattering cross section.

In the isotropic case, the response function may be averaged over all the orientations ψ (for detail, see the Appendix), that is,

$$\frac{d\Sigma_M}{d\Omega}(\mathbf{q},H_i)=S_H(\mathbf{q})R_{\rm iso}(\vartheta,q,H_i), \tag{18}$$

$$R_{\rm iso}(\vartheta,q,H_i)=\frac{1}{2\pi}\int_{-\pi}^{\pi}R(\psi,\vartheta,q,H_i)d\psi$$
$$=\frac{M_S^2}{2H_{\rm eff}^2}\left[1+\frac{\cos^2\vartheta}{\left(1+\frac{M_S}{H_{\rm eff}}\sin^2\vartheta\right)^2}\right]. \tag{19}$$

In the limit $H_{\rm eff}\gg M_S$, Eq. (19) suggests that $d\Sigma_M/d\Omega\propto 1+\cos^2\vartheta$, and independent of the value of $H_{\rm eff}$ the ratio r of the scattering cross section normal to the applied magnetic field over the scattering cross section parallel to the field has the value $\frac{1}{2}$.

The finding of enhanced scattering in the direction parallel to the magnetization contrasts with scattering by isolated ferromagnetic particles in a matrix, where the magnetic scattering cross section is enhanced in the direction normal to the magnetization, according to the well-known variation $d\Sigma/d\Omega\propto\sin^2\vartheta$.[29] In the latter case, the scattering contrast is due a jump in the *magnitude* of **M** at the interface between magnetic particle and nonmagnetic matrix, in other words, to a discontinuity of the component of the magnetization *parallel* to the field. By contrast, the scattering of interest in the present work is due to the nonuniform *orientation* of the magnetic moments (at constant magnitude of **M**). The spin misalignment gives rise to fluctuations in the component of **M** which is *normal* to the field.[5] The elastic scattering due to the static spin misalignment is similar to inelastic scattering by spin-waves in so far as the spin-wave scattering also follows the $(1+\cos^2\vartheta)$ law (see p. 53 in Ref. 36).

By averaging Eqs. (18) and (19) over the angle ϑ, one obtains the azimuthal average of the scattering cross section on a two-dimensional detector. When S_H is independent of ϑ then the result is

$$\frac{d\overline{\Sigma}_M}{d\Omega}(q,H_i)=S_H(q)\overline{R}(q,H_i), \tag{20}$$

$$\overline{R}(q,H_i)=\frac{M_S^2}{4H_{\rm eff}^2}\left[2+\frac{1}{\left(1+\frac{M_S}{H_{\rm eff}}\right)^{1/2}}\right]. \tag{21}$$

D. Measurement of A and of S_H

Based on the assumption that, near saturation, the residual and spin-misalignment scattering cross-sections are additive and using the fact that $d\Sigma_R/d\Omega$ is field independent near saturation, we have

$$\frac{d\overline{\Sigma}}{d\Omega}(q,H_i)=\frac{d\overline{\Sigma}_R}{d\Omega}(q)+S_H(q)\overline{R}(q,H_i). \tag{22}$$

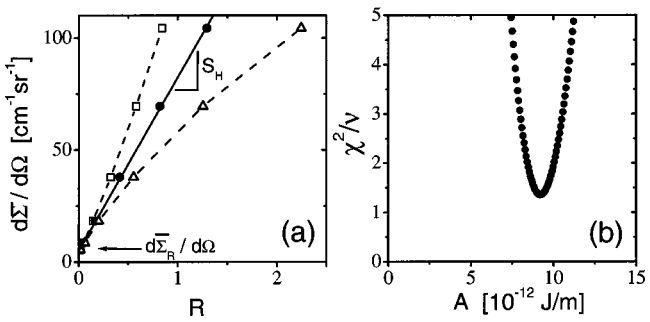

FIG. 2. (a) Experimental differential scattering cross section $d\overline{\Sigma}/d\Omega$ for nc Ni at $T=5$ K, $q=q_1=0.10\,\mathrm{nm}^{-1}$, and at different magnetic fields H_i, versus response function $\overline{R}(q_i,H_i)$. Values of H_i (in mT, and in order of decreasing R): 110, 240, 490, 990, 1990, 3990. The different symbols refer to computation of R with different values for the exchange-stiffness constant: $A=6.2\times10^{-12}$ J/m (△), 9.2×10^{-12} J/m (●), 12.2×10^{-12} J/m (□); the dashed lines are guides to the eye. The best straight-line fit (solid line) is obtained for $A=9.2\times10^{-12}$ J/m; the values of the anisotropy-field scattering function S_H and of the residual scattering cross-section $d\overline{\Sigma}_R/d\Omega$ at $q=q_1$ are given by the slope and the intercept of the line, respectively. (b) Reduced mean-square deviation between experiment and fit, χ^2/v, versus exchange-stiffness constant A for nc Ni at $T=5$ K.

For given values of A and M_S the response function $\overline{R}$ is known and the only unknowns in Eq. (22) are the functions $d\overline{\Sigma}_R/d\Omega$ and S_H. Since the equation is linear in $\overline{R}$, the values of these functions at any given experimental q can be determined by a straight-line fit in a plot of the experimental total scattering cross-section (measured at several magnetic fields) versus $\overline{R}(q,H_i)$ at that particular value of q; this is illustrated in Fig. 2(a). The data in the figure is for nc Ni at $T=5$ K, $q=0.10\,\mathrm{nm}^{-1}$, and is typical of our experimental results, details of which will be given below. It is emphasized that no underlying model is required for the functional dependence of S_H on q. Instead, the value of S_H at each experimental q is measured independently by the fit.

When the exchange-stiffness constant in the expression for $H_{\rm eff}$ is treated as an adjustable parameter, then the fit can also provide information on A, as illustrated in the figure: when $\overline{R}$ is computed with an arbitrary value of A, then $d\overline{\Sigma}/d\Omega$ depends nonlinearly on $\overline{R}$, contrary to Eq. (22). The ''true'' value of A is identified as that value for which the curvature vanishes. In the present work, a single value of A was used to fit simultaneously the entire data set, at all q and H_i, by Eq. (22) (one straight-line fit at each q). The experimental value of A was determined as that value that minimizes the weighted mean-square deviation χ between experiment and the simultaneous fit to all the data, with the weighting factors given, as usual, by the experimental uncertainty of the individual data points. As a measure of the uncertainty of the experimental value for A, we quote the bootstrap standard deviation, that is, the standard deviation of the set of results for A that is obtained by analysis of many samples with the same size as the actual data set, drawn

randomly from the data and allowing for multiple occurrence of individual data in the sample (see Ref. 37 for details).

It is noted that A is more generally computed from experimental values for a closely related quantity that governs the *dynamics* of the spin system, the spin-wave stiffness constant D. The most direct method for measuring D,*inelastic* neutron scattering, requires energy-resolved data from triple axes or time-of-flight instruments. Standard experimental SANS instrumentation measures an energy-integrated differential scattering cross-section and is therefore unable to discriminate between the elastic and the inelastic scattering. However, inelastic (magnon) scattering is restricted to scattering angles below a critical angle θ_C, and measurement of θ_C at $H=0$ provides an alternative way of measuring D based on SANS data,[38] in particular using polarized neutrons.[39] In nanocrystalline materials the accuracy of this method may be compromised by the strong elastic magnetic SANS background. In studies of the static magnetic microstructure one is interested in measuring the purely elastic magnetic SANS signal. In spite of the lack of energy resolution, this can be achieved by making use of the known fact that θ_C depends on the applied magnetic field,[40] and that spin-wave scattering is entirely suppressed at sufficiently high fields.[41] For the spin-wave dispersion relation $\hbar\omega = Dq^2 + g\mu_B\mu_0 H$, where $\hbar\omega$ denotes the spin-wave energy, it can be shown that the requirements of conservation of momentum $\mathbf{k}_0 = \mathbf{k}_1 + \mathbf{q}$ and energy $\hbar^2 k_0^2/(2m) = \hbar^2 k_1^2/(2m) + \hbar\omega$ cannot be satisfied simultaneously for any scattering vector in the small-angle regime when the field exceeds the critical value

$$H^* \approx \frac{\hbar^4 k_0^2}{4m^2 g \mu_0 \mu_B D} \tag{23}$$

(m, g, $\mathbf{k}_0$, and $\mathbf{k}_1$ denote, respectively, the neutron mass, the g factor, and the incident and scattered neutron wave vectors).[42] For $H \geqslant H^*$ the magnetic SANS is entirely elastic, as is required for analyzing the data in terms of our model.

The separation of $d\overline{\Sigma}_R/d\Omega$ and $d\overline{\Sigma}_M/d\Omega$ can be independently verified by experiments with a polarized neutron beam. Since the spin-misalignment scattering is independent of the polarization of the incident beam, the difference in the scattering cross sections for the two polarization states depends only on the residual scattering, and it is independent of the applied field. Equation (12) supplies the well-known result (compare, for instance, Ref. 43).

$$\frac{d\Sigma^-}{d\Omega} - \frac{d\Sigma^+}{d\Omega} = \frac{2}{V} b_{\mathrm{nuc}} b_{\mathrm{mag}} \sin^2\vartheta\, P_R(\mathbf{q}). \tag{24}$$

P_R denotes an interference function of the residual scattering, $P_R(\mathbf{q}) = \Sigma_{j,l} \exp[i\mathbf{q}(\mathbf{x}_j - \mathbf{x}_l)]$. In principle, P_R may be measured by the dependency of $d\Sigma/d\Omega$ on the polarization, provided that the nuclear and magnetic scattering-length densities in the defects that give rise to the residual scattering are known.

III. EXPERIMENT AND DATA REDUCTION

We investigated nanocrystalline Ni and Co samples prepared by pulsed electrodeposition (see details in Refs. 24 and 25); the samples are sheets with a thickness of 100–300 μm. Measurement by the Archimedes method indicated a mass density of $(100.0 \pm 0.2)\%$ of the literature value for the coarse-grained materials, suggesting low porosity and, hence, small residual scattering cross section. Hot extraction on the nc Ni sample yielded light elements impurities of 0.014 at. % hydrogen, 0.017 at. % nitrogen, and 0.0045 at. % oxygen. Nanocrystalline Ni prepared under identical conditions contains typically 0.1–0.3 at. % S and 0.1–0.2 at. % C.[44] As a reference material for the determination of the exchange-stiffness constant we used a polycrystalline Ni-sheet (purity: 99.99%) cold-rolled from 1 to 0.25 mm thickness.

X-ray scattering was recorded in Bragg-Brentano geometry with Mo $K\alpha_{1/2}$ radiation and a Si(Li) solid state detector. The magnetization isotherms were measured in a superconducting quantum interference device (SQUID) magnetometer. Rectangular rods typically $5 \times 2\ \mathrm{mm}^2$ were cut from the samples and mounted with the long axes parallel to the magnetic field. Both for the magnetization results and for the SANS data analysis, the magnetic field was corrected for demagnetization, with demagnetization factors estimated from the values for spheroids with aspect ratios similar to the samples. A typical value of N_d is 0.01 for the SANS samples, and the correction was found important only at small applied magnetic fields.

The Co sample for the SANS experiments was prepared by stacking two disks of 19 mm diameter and a total thickness of 160 μm, whereas the Ni sample was a single, 330-μm-thick sheet of similar lateral dimensions. The cold-worked sample consisted of a stack of four cold-rolled strips; in an effort to minimize the anisotropy in the plane the strips were mounted with the rolling direction rotated successively by 90° about the sample normal.

The ambient temperature SANS experiments were carried out at the 30-m SANS (NG3) instrument at the National Institute of Standards and Technology Cold Neutron Research Facility[45] (NCNR) with a wavelength $\lambda = 0.6$ nm and a wavelength spread $\Delta\lambda/\lambda = 0.15$. The samples were mounted on 12.7-mm-diameter Cd apertures and suspended between the pole pieces of an electromagnet with a maximum field of $\mu_0 H = 1.8$ T, oriented horizontally and normal to the incident beam. The field at the sample position was determined by a Hall probe and the lowest field, due to the remanence of the magnet, was found to be 1.3 mT. All SANS measurements were carried out with the sample first taken to the maximum field and the data then recorded at subsequently lower experimental fields. The runs with a non-polarized beam involved series of measurements with various magnetic fields at each of three different sample-to-detector distances, covering the q range of about 0.02–3 nm^{-1}. The data were corrected in the usual way for absorption, detector efficiency, and background, and were converted to absolute units with the aid of a porous SiO_2 standard. The sample transmission was measured for each field,

TABLE I. Results of Bragg-reflection profile analysis. L_{111} and L_{200}, area-weighted mean column lengths in the respective crystallographic direction. d_{area} and d_{volume}, area- and volume-weighted equivalent mean sphere diameters of the crystallites. α and β, stacking fault and twin fault probability, respectively. L_{fault}, estimated mean distance between faults. ε, estimated microstrain.

	L_{111} (nm)	L_{200} (nm)	d_{area} (nm)	d_{vol} (nm)	α	β	L_{fault} (nm)	ε (%)
nc Ni	11	6	49		$\leqslant 0.002$	0.05	4.3	0.4
nc Co				9.5 ± 3.0	0.1		1.9	$\leqslant 2.0$

but was found to increase only insignificantly, from 0.833 to 0.844 for the example of Ni, when the field was increased from 1.3 mT to 1.8 T.

The experiments with polarized neutrons at NIST used a supermirror transmission polarizer and a microwave spin-flipper in the primary beam; the polarization of the scattered neutrons was not discriminated. These experiments were only carried out at a single sample-detector distance, and were therefore restricted to the q range 0.08–0.7 nm^{-1}. The polarization of the incident beam, $p=|I^+-I^-|/(I^++I^-)$, was determined by measuring the transmission with a second supermirror inserted in the primary beam as the analyzer; I^+ and I^- denote the transmitted intensities with the spin-flipper on and off, respectively. The values of p were found to be 0.94 and 0.89 for the two spin orientations.

A SANS experiment with nc Ni at cryogenic temperatures was carried out at instrument V4 at the Berlin Neutron Scattering Center, using a nonpolarized beam and a 5-T cryomagnet with a vertical field. The sample was mounted on a 6-mm Cd aperture. The experimental procedure was analogous to the one at NCNR, with $\lambda = 0.6\,\text{nm}$, $\Delta\lambda/\lambda = 0.11$, and an estimated remanent field of 1 mT. Care was taken to correct for the comparatively strong scattering by the entrance and exit windows of the cryostate.

Materials parameters for Ni (Co in brackets) used in the data analysis are g factor $g=2.21(2.21)$, $\rho_a = 9.13 \times 10^{28}\,\text{m}^{-3}$ $(9.05\times 10^{28}\,\text{m}^{-3})$, $\mu_a = 0.616\mu_B(1.708\mu_B)$, hence $M_S = 522\,\text{kA/m}(1434\,\text{kA/m})$.[6]

IV. EXPERIMENTAL RESULTS

A. Wide-angle x-ray scattering

Planar defects, such as grain- and twin boundaries, are potential sources for discontinuities in the magnetic anisotropy field and it is therefore of interest to characterize the nature and number of these defects in the nanocrystalline samples. To this end, we analyzed wide-angle x-ray scattering data within the theoretical framework established by Warren.[46] Because of strong reflection overlap in Co, the more rigorous Warren-Averbach analysis[46] could only be applied to the Ni sample. An approximate analysis based on the integral width of the Bragg reflections[47] was applied in the case of Co. The results are summarized in Table I.

The x-ray scattering curves are displayed in Fig. 3. For Ni, the $\langle 200\rangle$ Bragg reflection is found to be wider than $\langle 111\rangle$, and consequently the value of the area-weighted mean column length in the $\langle 200\rangle$ crystallographic direction obtained by the Warren-Averbach analysis, L_{200}, is considerably smaller than the one for the $\langle 111\rangle$ direction, L_{111} (see Table I). This indicates that stacking faults or twin boundaries contribute to the broadening of the reflections.[46] The stacking fault probability α was determined by analysis of the reflection positions[46] and found to be insignificant. Therefore, the fault-induced broadening is dominated by the contribution from twin boundaries. The mean spacing between grain boundaries L and the twin boundary probability β was computed based on the experimental values for L_{111}, L_{200}, and α (see Sec. 13.5 in Ref. 46). An area-weighted mean grain size (based on an approximation of the grains as spheres) was obtained as $d_{\text{area}} = \frac{3}{2}L$,[48,49] and the mean distance between twin boundaries was estimated as $L_{\text{twin}} = d_{111}/\beta$ with d_{111} the $\langle 111\rangle$ interplanar spacing. While L_{111} and L_{200} are of the order of 10 nm the considerably higher value of 49 nm is found for the ''true'' grain size, d_{area}.[50] On the other hand, the mean distance between twin boundaries is estimated at only 4.3 nm, so that each grain contains several twin boundaries.

The scattering curve of nc Co, Fig. 3(b), indicates a hcp lattice structure, and the widths of the Bragg reflections are seen to be even more different than in Ni, with the $\langle 101\rangle$ and $\langle 201\rangle$ reflections considerably wider than the remaining ones. This is known to indicate a high density of stacking faults,[46] in agreement with the low stacking-fault energy of Co. A volume-weighted mean grain size d_{vol} (Refs. 47 and 49) was estimated by analysis of the integral breadth of those reflections that are exclusively broadened due to grain size and strain ($\langle 100\rangle$, $\langle 002\rangle$, $\langle 112\rangle$, $\langle 004\rangle$), and the stacking fault probability α was determined by using Eq. (13.85) in Ref. 46 in conjunction with mean column lengths estimated from the integral breadth of the $\langle 101\rangle$ reflection. The grain size is found to be quite small, about 10 nm, but the mean distance

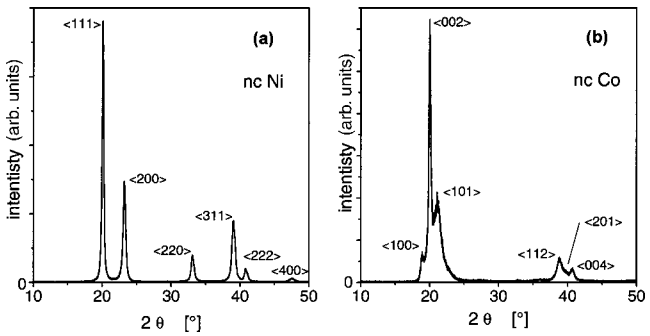

FIG. 3. X-ray diffraction intensity versus scattering angle 2θ for nc Ni (a) and nc Co (b).

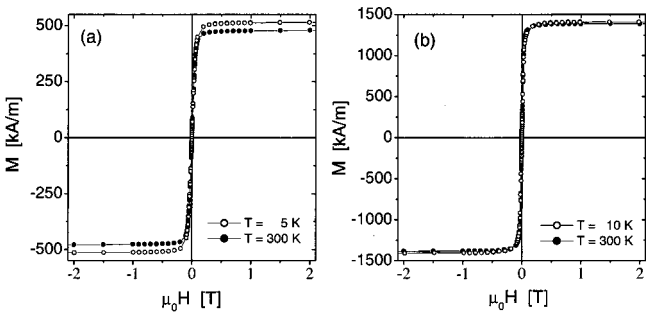

FIG. 4. Magnetization isotherms at $T=5$ and 300 K for nc Ni (a) and nc Co (b).

between faults, estimated as $L_{\text{fault}}=d_{002}/\alpha$ (with d_{002} the basal interplanar spacing), has an even smaller value of 1.9 nm.

Table I also lists values for the microstrain ε estimated from the scattering data.

B. Magnetization

Figure 4 shows magnetization isotherms for nc Ni and nc Co. It is seen, that the materials are nearly saturated at an applied field of about $\mu_0 H=0.2\,\text{T}$; the small-misalignment limit is therefore expected to be satisfied for this and higher fields. Estimates of the coercive field for nc Ni (nc Co in brackets) are $\mu_0 H_C=1.8\,\text{mT}(2.2\,\text{mT})$ at $T=5$ K and 0.2 mT (0.2 mT) at $T=300$ K. The coercivity values are of limited accuracy due to the hysteresis of the cryomagnet, but they show qualitatively that the samples are magnetically soft. High field extrapolations of the low-temperature isotherms, recorded up to a maximum field of 5.5 T, yielded saturation mass-magnetizations of 58.0(1) $\text{A m}^2/\text{kg}$ and 160.8(3) $\text{A m}^2/\text{kg}$ for Ni and Co, respectively, values that are within 1% and 2%, respectively, of the literature values[6] of 58.57 $\text{A m}^2/\text{kg}$ for coarse-grained Ni and 163.1 Am^2/kg for coarse-grained hcp Co. This confirms recent results for the saturation magnetization in electrodeposited nc Co, Ref. 51.

C. Unpolarized SANS

The experimental $d\bar{\Sigma}/d\Omega$ from the unpolarized runs, recorded at different combinations of magnetic field and temperature, are displayed in Fig. 5. The scattering cross section is seen to diminish strongly when the magnetic field H is increased, in the case of nc Ni and nc Co at $T=295\,\text{K}$ by close to three orders of magnitude. Although the samples are nearly saturated at $\mu_0 H=0.2\,\text{T}$, $d\bar{\Sigma}/d\Omega$ continues to vary as a function of H throughout the experimentally accessible range of applied fields, which extends to the much higher values of 1.8 T for the ambient temperature runs and 4 T at cryogenic temperature. This suggests that the scattering signal is dominated by the progressive alignment of magnetic moments in the nearly saturated ferromagnet, as investigated by the theory in Sec. II. The strongly field-dependent signal cannot originate from magnetized particles in a nonmagnetic matrix (or from nonmagnetic particles or pores in a magnetic matrix), since the scattering contrast between a particle and the matrix would remain essentially constant, independent of H, once the sample was near saturation. It is also seen that the region of maximum curvature in the log-log plots of $d\bar{\Sigma}/d\Omega$ versus q is shifted to larger q as the field is increased. In SANS data the scattering vector at maximum curvature often corresponds to 2π over a characteristic length scale; therefore the observation is consistent with the notion (compare Sec. II A) that increasing the magnetic field leads to a suppression of the long-wavelength magnetic fluctuations of the magnetization, so that the dominant wavelength is progressively reduced.

In order to verify the elastic nature of the SANS signal, comparative measurements with wavelengths $\lambda=0.6$ and 1.1 nm were performed on the nc Co sample at $T=295\,\text{K}$. Figure 6 shows that the differential scattering cross section is a function of $4\pi\sin(\theta)/\lambda$, where the scattering angle is 2θ. This is not expected for inelastic scattering and confirms the elastic nature of the scattering signal.

As an illustration of the azimuthal anisotropy of the scattering pattern on the area detector, Fig. 7, shows the field

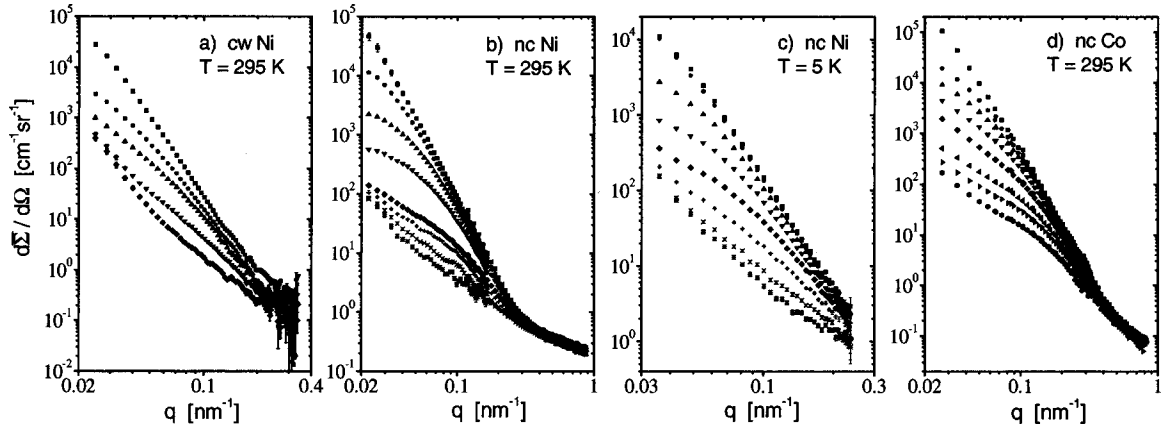

FIG. 5. Experimental differential scattering cross section $d\bar{\Sigma}/d\Omega$ versus modulus q of the scattering vector for different magnetic fields and for (a) cw Ni, (b) nc Ni at 295 K, (c) nc Ni at 5 K, and (d) nc Co. Values of the magnetic field $\mu_0 H_i$ [from top to bottom (mT)]: (a) 5, 87, 190, 570, 1710; (b) 0.5, 39, 88, 190, 570, 800, 1240, 1790; (c) 0.5, 40, 110, 240, 490, 990, 1990, 3990; (d) 5, 43, 87, 180, 390, 770, 1140, 1740.

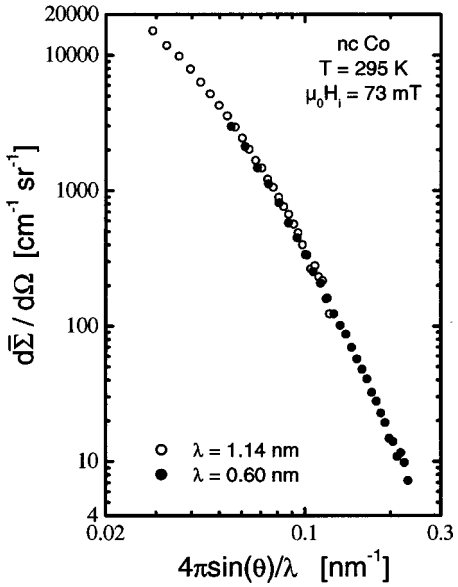

FIG. 6. Azimuthal average differential scattering cross section $d\bar{\Sigma}/d\Omega$ for nanocrystalline Co at $T=295$ K measured with wavelengths of 0.6 nm (solid circles) and 1.14 nm (open circles), plotted as a function of $q=4\pi\sin(\theta)/\lambda$. The good agreement between the two data sets indicates that the scattering is elastic.

dependence of the ratio r of scattering cross section normal to the applied magnetic field to the cross section parallel to the field at scattering vector $q=0.1\,\mathrm{nm}^{-1}$. r was determined as the ratio of $\pm 15°$ sector (ϑ) averages of $d\Sigma/d\Omega$ in the respective directions and at the particular scattering vector; examples for the full q dependence can be found in the display of the polarized scattering data, Fig. 8 below. Two data sets, nc Ni at $T=5$ K and nc Co at $T=295$ K, show $r<1$ in agreement with the theoretical result for spin-misalignment scattering [see Eq. (19)]. The results for cold-worked Ni and for nc Ni at $T=295$ K have $r>1$, in disagreement with the theory.

D. Polarized SANS

Figure 8 displays results obtained with polarized neutrons for the Co sample at ambient temperature. The closed symbols refer to $\pm 15°$ sector averages of the scattering cross section for *q parallel* to the applied field, whereas the open symbols refer to analogous averages for *q normal* to the applied field. Circles and triangles denote the two spins states, but $d\Sigma/d\Omega$ varies very little when the incident neutron spin is flipped, and the difference is not resolved in the figure, except at the highest applied field, where the total scattering intensity is small. The difference between the spin up and spin down values of $d\Sigma/d\Omega$ for q normal to the field, $\Delta d\Sigma/d\Omega$, is plotted in Fig. 9, for nc Ni and nc Co. It is seen that $\Delta d\Sigma/d\Omega$ is much smaller than $d\Sigma/d\Omega$, and that $\Delta d\Sigma/d\Omega$ is independent of H. As discussed in Sec. II B the polarization dependence of $d\Sigma/d\Omega$ originates from interference between magnetic and nuclear scattering. Since the scattering due to spin misalignment varies strongly as a function of H, the finding of a field-independent $\Delta d\Sigma/d\Omega$ can only be understood if there is no interference between the nuclear and spin-misalignment scattering amplitudes. Therefore, the result supports the assumption, underlying the discussion in Secs. II B and II D, of negligible interference between spin-misalignment scattering and residual scattering,

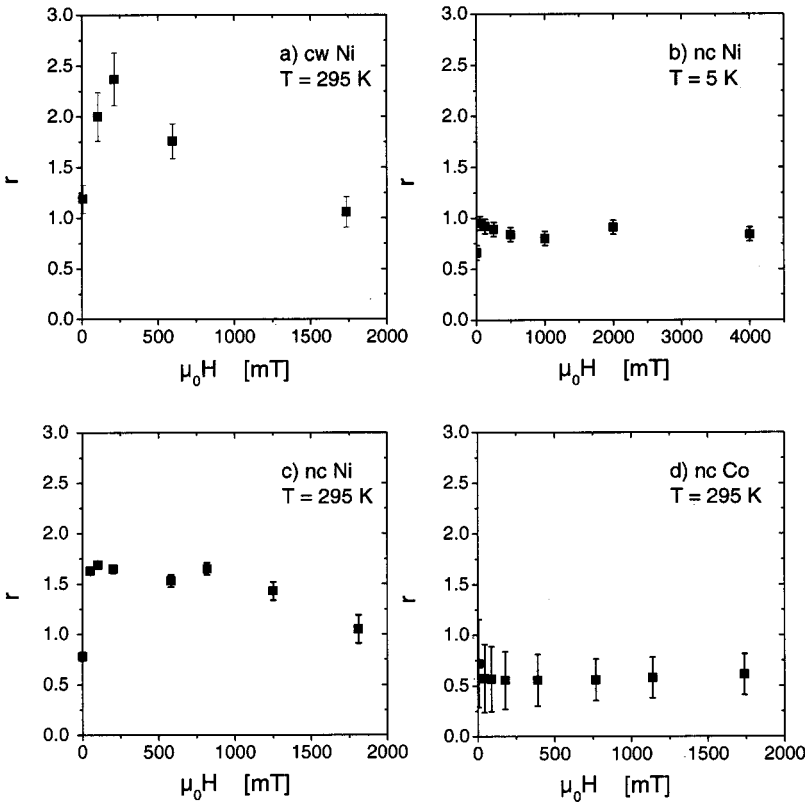

FIG. 7. Azimuthal anisotropy of the experimental differential scattering cross section versus internal magnetic field H_i, evaluated at $q=0.1\,\mathrm{nm}^{-1}$. r denotes the value of the scattering cross section for q normal to the field over the one for q parallel to the field.

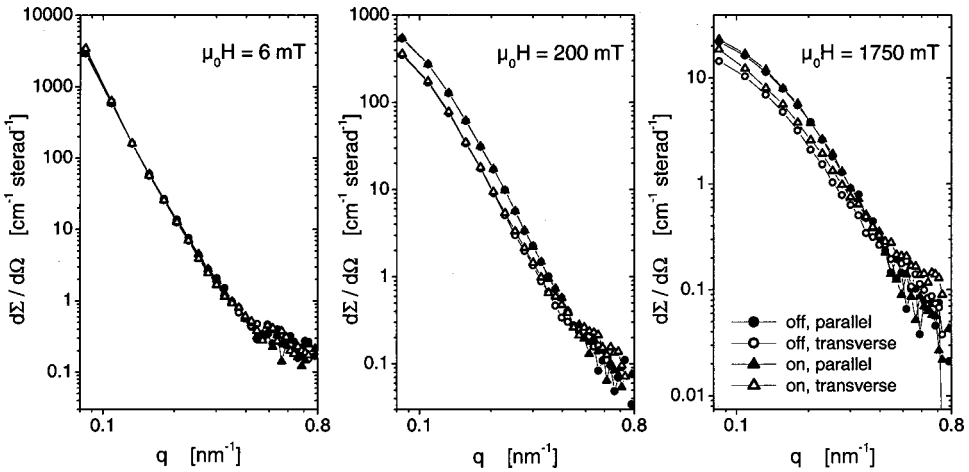

FIG. 8. Results of polarized scattering runs for nc Co at applied magnetic fields of $\mu_0 H = 6$, 200, and 1750 mT as indicated in the figure. The data are $\pm 15°$ sector averages of the differential scattering cross section parallel (full symbols) and transverse (open symbols) to the field direction with spin-flipper off (circles) and on (triangles). Temperature $T = 295$ K.

and it suggests that the interference is related to the small residual scattering cross section from pores or second phases.

For nc Ni the values of $\Delta d\Sigma/d\Omega$ at the lowest applied field (6 mT) are found to be nearly zero, in other words, $d\Sigma/d\Omega$ is practically independent of the incident polarization. This can be attributed to the deviation from the magnetically nearly aligned state and to the formation of a magnetic domain structure, which may result in depolarization.[52]

V. DISCUSSION

A. Small misalignment criterion

We have noted that the dependency of the azimuthal average differential scattering cross section on the applied magnetic field and on the scattering vector is in qualitative agreement with the predictions of the theory for scattering due to spin misalignment. For nc Ni at $T = 5$ K and for nc Co at $T = 295$ K, the dependence of $d\Sigma/d\Omega$ on the azimuthal angle ϑ is also in agreement with the theory, with the differential scattering cross section enhanced in the direction parallel to the applied field ($r < 1$). This supports that the scattering originates from small fluctuations of the magnetization direction in a material with otherwise uniform and aligned magnetization. By contrast, for cw Ni and for nc Ni at $T = 295$ K the differential scattering cross section is enhanced in the direction normal to the applied field ($r > 1$), up to the highest field investigated; this suggests that $d\Sigma/d\Omega$ is here dominated by the scattering contrast from moments that cannot be aligned even with an applied field of 1.8 T. It is known that ''exchange anisotropy'' due to antiferromagnetic coupling at metal-oxide interfaces in isolated particles[53] and nanocrystalline materials[54] can strongly pin the magnetization. However, the total oxygen content in the nanocrystalline Ni sample was found to be quite low (0.0045 at. %, compare Sec. III), and scattering runs with an annealed Ni sheet from the same batch as the cold worked sample had $r < 1$ and a much smaller scattering cross-section than cw Ni; therefore the finding of $r > 1$ appears not to be due to exchange bias at oxide inclusions.

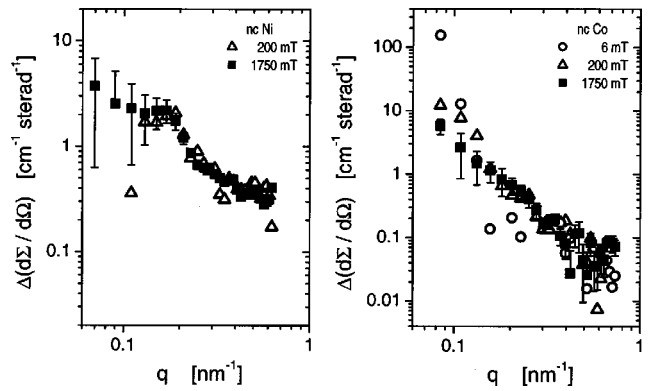

FIG. 9. Difference $\Delta d\Sigma/d\Omega$ between the differential scattering cross sections with the spin flipper on and off, respectively, measured in the direction normal to the applied magnetic field. Diagram on the left, nc Ni; on the right, nc Co. Different symbols refer to different applied magnetic fields as indicated in the figure. Temperature $T = 295$ K.

A possible alternative explanation for the strongly pinned moments is that the changes of the local atomic coordination and spacing in the core of defects, such as dislocations or grain boundaries, may induce either very high local values of the magnetic anisotropy or even local antiferromagnetic coupling. A large anisotropy at grain boundaries would have analogies in the surface anisotropy in isolated nanoparticles. Because the exchange interaction suppresses discontinuous changes in the spin orientation, the local canting of the atomic spin at defects would entail extended gradients of the misalignment in the surrounding matter; such gradients obey Eq. (2) and will therefore give rise to SANS with a field-dependence similar to that discussed in Sec. II C.

The evolution from $r > 1$ to $r < 1$ upon cooling nc Ni may be understood as a result of the temperature dependence of the magnetocrystalline anisotropy, which increases in magnitude by a factor of about 20 (in single crystals)[6] between 295 and 5 K, thereby increasing the spin misalignment throughout the entire sample and enhancing the scattering from those micromagnetics fluctuations that are considered in the model.

B. Exchange-stiffness constant

We shall now assess the model by discussing results for the exchange stiffness constant A and for the anisotropy field

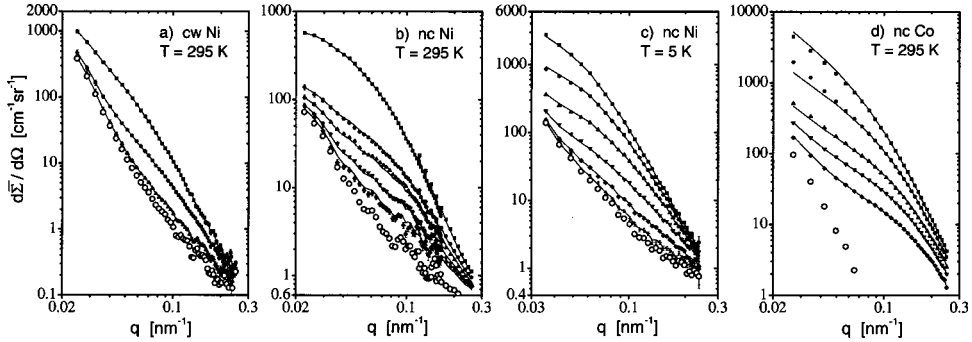

FIG. 10. Fit (lines) to the experimental data (●) of Fig. 5 based on Eq. (22); the lines connect the values of $d\bar{\Sigma}^{\mathrm{Fit}}/d\Omega$ at the discrete experimental q and H_i. The data at the lowest applied fields may contain inelastic scattering and are therefore ignored. The values of the remaining magnetic fields are as in Fig. 5. The open circles (lowest curve in each plot) represent the residual scattering cross sections $d\bar{\Sigma}_R/d\Omega$.

scattering function S_H obtained by fitting the experimental $d\bar{\Sigma}/d\Omega$ obtained with an unpolarized neutron beam by the micromagnetics model, as discussed in Sec. II D. We shall examine all four data sets, bearing in mind that a prerequisite of the model, the small misalignment approximation, is only satisfied in nc Co at $T=295$ K and in nc Ni at $T=5$ K, whereas it is, at least locally, violated in nc Ni and cw Ni at $T=295$ K. Literature data for the spin-wave stiffness constant D, which are confirmed by our independent determination (see below), suggest the estimates for the field required to suppress magnon scattering [Eq. (23)], $H^*=90$ mT for Ni and $H^*=70$ mT for Co; in order to guarantee that the scattering is elastic, only data recorded at fields $\geqslant H^*$ were considered in the analysis. The fits were also limited to data at $q \leqslant q^* = \sqrt{\mu_0 M_S H_{\max}/(2A)}$ with $H_{\max}$ the largest applied magnetic field, because Eqs. (6) and (7) predicts that the effective field H_{eff} will show no significant dependence on the applied magnetic field H for $q > q^*$. By inspection of Eqs. (20) and (21) it is seen that $d\bar{\Sigma}/d\Omega$ is then practically independent of H, with the consequence that no reliable separation between spin misalignment scattering and residual scattering is possible for $q > q^*$.

Figures 10(a)–10(d) display the experimental $d\bar{\Sigma}/d\Omega$ for unpolarized neutron beam (compare Fig. 5) together with the best fits by Eq. (22). It is seen that for all specimens and throughout the entire experimental range of magnetic fields and scattering vectors, the fit reproduces the dependency of $d\bar{\Sigma}/d\Omega$ on the scattering vector and on the magnetic field, in good agreement with the data. In accordance with that observation, the minimum values in the reduced mean-square deviation between experiment and fit, $\chi^2(A)/v$ (where v refers to the number of degrees of freedom)[55] are found to be of the order of unity, supporting the validity of the model. The well-defined minimum in χ^2/v is illustrated in Fig. 2(b) for the example of nc Ni at $T=5$ K. The values of A inferred from the minima in $\chi^2(A)$ are displayed in Table II.

TABLE II. Ferromagnetic exchange-stiffness constant A and spin-wave stiffness constant D determined by analysis of the SANS data.

	cw Ni	nc Ni		nc Co
T (K)	295	5	295	295
A (10^{-12} J/m)	8.2 ± 0.2	9.2 ± 0.2	7.6 ± 0.3	28 ± 1
D (meV Å^2)	400 ± 10	450 ± 10	370 ± 20	500 ± 20

The spin-wave stiffness constant D is related to A via $D=2Ag\mu_B/(\rho_a\mu_a)$,[22] and the results for D inferred from our data are also shown in Table II. Previous measurements of D by inelastic neutron scattering on single-crystal samples yielded $D=374\pm20$ meV Å^2, $D=433$ meV Å^2, and $D=420$ meV Å^2 for Ni,[56–58] and $D=490\pm20$ meV Å^2 for hcp Co.[59] It is seen that our results are in excellent agreement with the literature data. The observed increase in A (and D) of nc Ni by (21 ± 5) % of the ambient temperature value between 295 and 5 K is comparable to a reported increase by 31% in single crystals.[58]

Comparing the experimental value of A in nanocrystalline materials to that of coarse-grained polycrystalline or single-crystal samples is of interest since analytical[14] and numerical[13] models indicate that a local reduction of A at internal interfaces can significantly increase the coercivity and reduce the remanence in nanocrystalline ferromagnets and in ferromagnetic nanocomposites where the grains are separated by an interfacial phase with magnetic properties that differ from those of the grains. Our result for A in nc Ni is somewhat smaller than that in cw Ni, but since the difference is comparable to the experimental error the results are compatible with the assumption of a uniform value of A that underlies our theory. In other words, we find no conclusive evidence for a local reduction of A at grain boundaries in Ni and Co.

C. Residual scattering cross section

Also shown in Fig. 10 is the residual scattering cross section determined from the fits to the experimental data. It is seen that the total scattering is significantly above the residual scattering even at the highest applied field, suggesting that there may be significant spin-misalignment scattering even in samples that are considered saturated in common SANS data analysis.

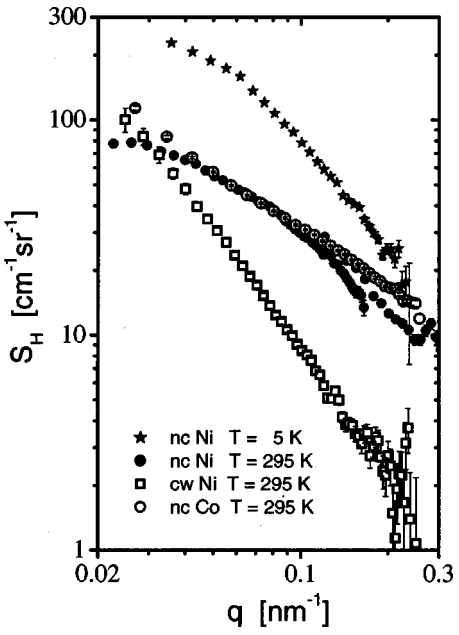

FIG. 11. Log-log plot of the anisotropy field scattering functions $S_H(q)$ determined from the fits in Fig. 10.

For Co the computed $d\overline{\Sigma}_R/d\Omega$ is zero within error bars for $q>0.1\,\mathrm{nm}^{-1}$. This is unphysical since the true $d\overline{\Sigma}_R/d\Omega$ cannot be smaller than the nuclear incoherent scattering cross section. The finding suggests qualitatively that $d\overline{\Sigma}_R/d\Omega$ is considerably smaller than the total experimental scattering cross section at the highest applied magnetic field; in other words, the spin-misalignment scattering is dominant at all applied fields, and a much higher field would have been necessary to suppress the spin-misalignment scattering sufficiently for the weak residual scattering to be resolved. It is noted that the difference cross section of the polarized data for nc Co, Fig. 9 above, is also considerably smaller than the total cross section of that sample at the highest applied field. Since the difference cross section scales with the residual scattering cross section, compare Eq. (24), this result supports qualitatively the conclusion that, for $q>0.1\,\mathrm{nm}^{-1}$, $d\overline{\Sigma}_R/d\Omega$ in nc Co is small compared to the spin-misalignment scattering

D. Anisotropy field scattering function

Besides separating the spin-misalignment scattering from residual scattering, the fits to the scattering data by Eq. (22) also yield the anisotropy field-scattering function $S_H(q)$. Except for a dependency on known materials parameters, S_H depends only on the Fourier coefficients of the anisotropy field $\mathbf{H}_P(\mathbf{x})$; because of the formal similarity of the defining equation for S_H, Eq. (16), to the corresponding expressions for nuclear scattering the established procedures for characterizing the nuclear microstructure from experimental nuclear SANS cross sections can be used analogously to obtain information on $\mathbf{H}_P(\mathbf{x})$.

Figure 11 displays the results for $S_H(q)$. For cw Ni, S_H can be approximated by a power law in q with an exponent -1.9 in the entire q range. The results for the nanocrystalline samples have a weaker dependence on q, and it can be seen that S_H for the nc Ni sample decreases when the temperature is increased. It has been proposed that the volumetric mean square anisotropy field can be computed from the experimental S_H based on an invariant of the anisotropy field scattering function:[22]

$$\langle|\mathbf{H_P}|^2\rangle_V=\frac{M_S^2}{2\pi^2 b_{\mathrm{mag}}^2\rho_a^2}\int_0^\infty S_H(q)q^2dq. \tag{25}$$

Evaluation of the integral in the restricted interval of q accessible to experiment (compare Fig. 11) yields a partial invariant and, thereby, suggests lower bounds for the mean-square anisotropy field; the results for this quantity are displayed in Table III.

For the idealized case of a saturated, texture-free polycrystal where only magnetocrystalline anisotropy is present, the value of $\langle|\mathbf{H}_P|^2\rangle_V$ can be computed as follows: at saturation, the magnetization is aligned with the applied field throughout the material, whereas the crystallographic easy axes of the individual grains are randomly oriented in space. This means that the magnetization takes on all orientations relative to the crystallographic axes with equal probability. The expectation value for $|\mathbf{H}_P|^2$ in the saturated polycrystal can therefore be computed by averaging $|\mathbf{H}_P|^2$ in a single crystal over all orientations of $\mathbf{M}$ relative to the crystallographic axes. In other words, the volumetric mean-square anisotropy field $\langle|\mathbf{H}_P|^2\rangle_V$ in the polycrystal coincides with the orientation mean square anisotropy field $\langle|\mathbf{H}_P|^2\rangle_\Omega$ of a single-crystal. Table III displays $\langle|\mathbf{H}_P|^2\rangle_\Omega$ computed from literature data for the dependency of the anisotropy energy on the crystallographic orientation in single crystals.[6]

It is seen that the experimental bound for $\langle|\mathbf{H}_P|^2\rangle_V$ in all Ni data sets is larger than the theoretical $\langle|\mathbf{H}_P|^2\rangle_\Omega$. This may be understood as a result (i) of the contribution of magnetoelastic anisotropy to H_P on top of the magnetocrystalline

TABLE III. Lower bounds for the volumetric root-mean-square (RMS) anisotropy field $\langle|\mathbf{H}_P|^2\rangle_V^{1/2}$, determined from the partial invariant of the anisotropy field scattering function $S_H(q)$. The columns labeled Ni (cryst) and Co (cryst) refer to the orientation-averaged RMS magnetocrystalline anisotropy field $\langle|\mathbf{H}_P|^2\rangle_\Omega^{1/2}$ in single crystals of Ni and Co, respectively, and were computed from data in Ref. 6.

	cw Ni	nc Ni		nc Co	Ni (cryst)		Co (cryst)
T (K)	295	5	295	295	4.2	296	288
$\mu_0\langle|\mathbf{H}_P|^2\rangle_V^{1/2}$ (mT)	43	126	92	101			
$\mu_0\langle|\mathbf{H}_P|^2\rangle_\Omega^{1/2}$ (mT)					93	4	320

anisotropy, and (ii) of the existence, inferred from the azimuthal anisotropy of $d\Sigma/d\Omega$, of additional scattering from spin canting that decorates pinning centers at defects. In fact, the agreement is best for nc Ni at $T=5$ K, were the magnetocrystalline anisotropy is strong and is therefore expected to contribute dominantly to $\langle|\mathbf{H}_P|^2\rangle_V$. A similar enhancement of the anisotropy constant, relative to the value in the coarse-grained material, has also been inferred by analysis of the approach to saturation in nc Fe.[54]

For nc Co at 295 K the experimental lower bound for $\langle|\mathbf{H}_P|^2\rangle_V$ is smaller than the theoretical $\langle|\mathbf{H}_P|^2\rangle_\Omega$. In fact, the experimental $S_H(q)$ of all samples diminish more slowly than q^{-2}, so that the integral in Eq. (25) shows no sign of convergence within the experimental interval of q, limited to $q_{\max}=0.3\,\mathrm{nm}^{-1}$. This suggests that important contributions to the integral are at q values higher than 0.3 nm^{-1}, corresponding to structures smaller than roughly $2\pi/q_{\max}$ ≈ 20 nm. This agrees with the finding of the x-ray analysis that the grain size of Co is only about 10 nm, and that the distance between twin boundaries or stacking faults are even smaller, about 4 and 2 nm in Ni and Co, respectively. In Ni, twin boundaries are on $\langle 111\rangle$ planes, and the easy axes is along the $\langle 111\rangle$ lattice directions. It is readily verified that three out of four easy axes are discontinuous at any twin boundary and that, unless the magnetization is aligned with the fourth direction (i.e., along the twin boundary normal), the anisotropy field will also be discontinuous. Therefore, the large number of twin boundaries in nc Ni leads to nonuniformity of the anisotropy field on a scale much smaller than the grain size, which cannot be resolved in $S_H(q)$ due to the finite $q_{\max}$. In Co, twin boundaries and stacking faults are on the basal planes, and the easy axes is along the normal of the basal planes. Here, the easy axes is continuous at the planar defect, so that there will be no long-range inhomogeneity of the anisotropy field. However, the presence of defects may lead to localized nonuniformity of the anisotropy in the immediate vicinity of the defect.

Straight lines fitted to the low-q part of the data in a plot of $\ln S_H$ versus q^2 (Guinier plot) have the slope $r_G/3$ with r_G the radius of gyration.[60] Similar to nuclear scattering, where r_G is a measure for the particle size, r_G deduced from the anisotropy field-scattering function is a measure for the size of regions in which the anisotropy field is aligned parallel.[22] In an idealized nanocrystalline ferromagnet with purely magnetocrystalline anisotropy, the radii of gyration of the crystallites and of the anisotropy field will coincide. We could not evaluate r_G for nc Co since the Guinier plot does not give a straight line, but for nc Ni the plot, Fig. 12, is approximately linear and the fits suggest $r_G=20$ nm at $T=5$ K and $r_G=22$ nm at $T=295$ K. For idealized spherical grains of diameter d the radius of gyration is $r_G=(\frac{3}{5})^{1/2}d/2$, in other words, $r_G=19$ nm would be inferred from the x-ray result $d=49$ nm, in apparent agreement with the results obtained from S_H. Note that when there is a set of objects with a distribution of sizes, then the experimental r_G is heavily weighted towards the largest objects.[61] Our result for r_G in nc Ni is therefore compatible with our earlier conclusion that the anisotropy field also exhibits additional structure on a much smaller scale than 20 nm.

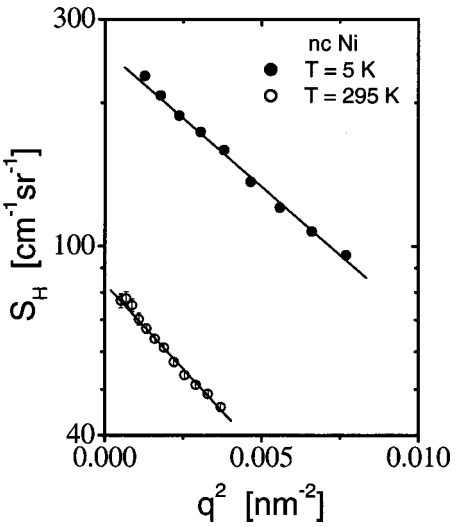

FIG. 12. Log-linear plot of the low-q part of $S_H(q)$ versus q^2 (Guinier-plot of S_H) for nc Ni at $T=5$ K (●) and at $T=295$ K (○). The solid lines are the straight lines of best fit to the data.

E. Validity of the model at small magnetic field

Despite the lack of rigorous justification for doing so it is of interest to compare the predictions of Eqs. (20)–(22) to the experiment at small applied magnetic field where the mean misalignment angle of the magnetization is not small. To this end, Fig. 13 displays the scattering data for Co in the complete range of scattering vector and field together with the model. The parameters of the fit are the same as in Fig. 10(d), in particular, only data recorded at magnetic fields

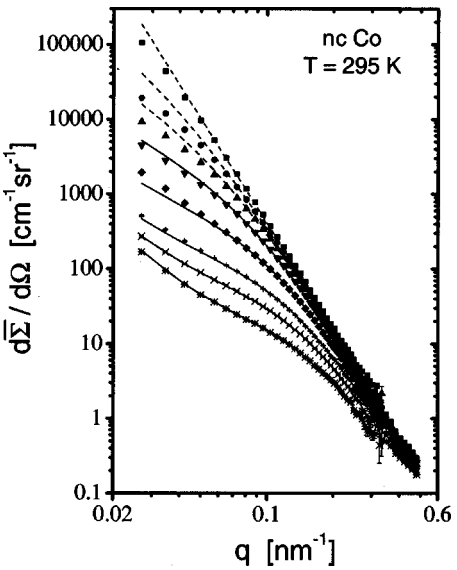

FIG. 13. Symbols, experimental azimuthal average differential scattering cross section $d\bar{\Sigma}/d\Omega$ for nc Co at $T=295$ K as in Fig. 5(d). Solid lines, fit to the data at magnetic fields $\mu_0 H_i \geqslant 180$ mT, as in Fig. 10; dashed lines, extrapolation to data recorded at smaller magnetic fields.

$\mu_0 H_i \geqslant 180\,\mathrm{mT}$ are considered in computing $S_H(q)$ and $d\bar{\Sigma}_R/d\Omega(q)$. Based on that fit, the figure also displays the $d\bar{\Sigma}/d\Omega$ computed by extrapolation to the smaller internal fields of $\mu_0 H_i = 2.3$, 46, and 91 mT. It is seen that the extrapolated data practically interpolate the experiment for $q > 0.06\,\mathrm{nm}^{-1}$, and that there is qualitative agreement at lower q. This supports the finding from the Ni data at 295 K, that Eqs. (20)–(22) appear to give a good description of the field dependence of the scattering even when the misalignment angle is not small.

In the interval $0.1 \leqslant q \leqslant 0.2\,\mathrm{nm}^{-1}$ the experimental $d\bar{\Sigma}/d\Omega$ of nc Co at the lowest applied field is well approximated by a power law in q with an exponent of $-4.7(1)$. The corresponding values for cw Ni and nc Ni at $T = 295$ K, and for nc Ni at $T = 5$ K are $-5.0(1)$, $-4.9(1)$, and $-4.9(1)$, respectively. It is noted that the steepest power law predicted by the models based on noninterfering hard spheres with a distribution of sizes, used in previous data analysis of magnetic SANS,[18,19] is the well-known q^{-4} law. Therefore, such models do not apply to the present data. By contrast, Eqs. (20) and (21) can readily explain steep power laws for the spin-misalignment scattering: when the magnetocrystalline anisotropy is dominant then $S_H(q)$ has an asymptotic q^{-4} decay at large q,[22] and by Eqs. (6) and (21) the response function R varies also asymptotically as q^{-4}. Since the scattering cross section is the product of S_H and R, the asymptotic power law may be as steep as q^{-8}.

VI. CONCLUSIONS

We have analyzed the field dependent elastic SANS data recorded on nanocrystalline and cold-worked polycrystalline Ni and Co near saturation in terms of a model derived from micromagnetics theory in the limit of small misalignment of the magnetization. We have found good agreement between theory and experiment for the samples with the highest magnetocrystalline anisotropy (Co at ambient and Ni at low temperature). For Ni, both nanocrystalline and cold-worked polycrystalline, at ambient temperature some spins retain a finite misalignment to the applied magnetic field even at the highest fields available; therefore the requirement for the applicability of the theory is not strictly satisfied. However, we find that for all samples the variation of the azimuthal average scattering cross sections with the scattering vector and the applied field can be excellently fitted by the theory. Moreover, the results for the ferromagnetic exchange constant are in good agreement with the published data determined by inelastic neutron scattering on single crystals. It is concluded that, where the small-misalignment limit can be reached, the theoretical predictions are well supported by experiment. When the misalignment of some spins remains finite, there is no rigorous justification for applying our analysis, but the experiment remains, at least qualitatively, in agreement with the theory, suggesting that the linearized solution to the balance of torque equation [Eq. (2)] may still provide a useful approximation. It is emphasized that the analysis is not restricted to nanocrystalline materials, but that it applies quite generally to bulk ferromagnets with an anisotropy that is nonuniform on a nanometer scale. This includes, in particular, amorphous ferromagnets with ''random'' [62] anisotropy.

The SANS data confirm the prediction of micromagnetics theory that near saturation the magnetic microstructure on the scale of 1 nm to several hundred nm may be described as interpenetrating static fluctuations of the orientation of the magnetic moments about the field direction; as the field is decreased both the amplitude and the dominant wavelength of the fluctuations increases. It has been suggested that magnetic SANS data from nanocrystalline solids can be analyzed in terms of scattering by noninterfering hard spheres.[18,19] This presupposes that the magnetic microstructure is validly described by an array of domains with uniform scattering contrast (uniform magnetization), with discontinuous jumps of the magnetization at the domain boundaries. Such domains are indeed generally observed in nanocrystalline soft magnets, but their dimensions are on the scale of microns or above,[63] beyond the resolution of SANS. Our considerations show that the SANS signal arises not from the domain structure, but from the continuous variation of the spin misalignment angle, which defines the *internal* structure of domains and which is not adequately described by hard-sphere models.

Finally, our data are in support of magnetic properties of elemental nanocrystalline ferromagnets depending not only on the grain size d; instead, we infer that other factors besides d can significantly affect the magnetic microstructure, in particular, twin boundaries and centers of strong anisotropy or of antiferromagnetic coupling, potentially due to changes in the atomic coordination and interatomic spacing in the core of grain boundaries or dislocations.

ACKNOWLEDGMENTS

This work was supported by the Alexander von Humboldt-Foundation (Feodor Lynen program), by the Deutsche Forschungsgemeinschaft (SFB 277 and Heisenberg-Programm), by the National Science Foundation (Agreement No. DMR-9423101), and the European Commission (TMR Contract No. ERB FMGECT 950060).

APPENDIX: RESPONSE FUNCTION FOR SANS BY ANISOTROPIC MICROSTRUCTURES

The results of Sec. II C involve the restrictive assumption of an isotropic microstructure, an assumption that must *a priori* be questioned for the cold-worked and, therefore, textured samples, which are considered as part of the present study. In fact, typical samples for magnetic SANS will often exhibit a sheet geometry, for instance, thin films or sheets deposited from vapor or solution or melt-spun ribbons; while it may be admissible to approximate the microstructure of such samples as isotropic in the plane, an out-of-plane anisotropy must be admitted since the sheet or film normal is generally a preferred direction (growth direction or direction of solidification). We shall now compute $d\Sigma_M/d\Omega$ of a sample in which the distribution of the directions of the magnetic anisotropy field exhibits preferred orientations. To this

end, we assume that the Fourier coefficients of the anisotropy field can be expressed as $\mathbf{h}(\mathbf{q})=\Sigma_j \mathbf{h}_j(\mathbf{q})$ with the $\mathbf{h}_j(\mathbf{q})$ originating from individual grains or defects, and consider only such cases where the directions of the anisotropy fields of the individual defects are uncorrelated, so that terms $\mathbf{h}_i(\mathbf{q})\cdot\mathbf{h}_j(\mathbf{q})$ with $i\neq j$ take both signs with equal probability. Consequently, the expectation value for the sum over these terms vanishes, and

$$|\mathbf{h}(\mathbf{q})|^2=\sum_j |\mathbf{h}_j(\mathbf{q})|^2. \tag{A1}$$

Because **m** and **p** are linear vector functions of **h** and **m**, respectively, Eqs. (A1) and (5) imply that

$$|\mathbf{m}(\mathbf{q})|^2=\sum_j |\mathbf{m}_j(\mathbf{q})|^2,$$

$$|\mathbf{p}(\mathbf{q})|^2=\sum_j |\mathbf{p}_j(\mathbf{q})|^2,$$

$$\frac{d\Sigma_M}{d\Omega}(\mathbf{q},H_i)=\sum_j S_{H,j}(\mathbf{q})R(\psi_j,\vartheta,q,H_i), \tag{A2}$$

with $S_{H,j}(\mathbf{q})=8\pi^3 V^{-1} b_{\mathrm{mag}}^2 \rho_a^2 M_S^{-2} h_j(\mathbf{q})^2$ [compare Eq. (16)]. Note, that the decomposition of the anisotropy field Fourier transform $\mathbf{h}(\mathbf{q})$ into contributions from individual ''defects'' does not require that the corresponding structures in real space be spatially separated; these contributions will overlap, for instance, when magnetoelastic anisotropy due to long-range strain fields from dislocations is considered. Because perturbations of the spin-structure decay on a length scale l_H, the perturbations of the magnetization resulting from the individual $\mathbf{h}_j(\mathbf{q})$ will quite generally overlap, even when the anisotropy fields of the microstructural elements are localized as in the case of the magnetocrystalline anisotropy of the individual grains in a polycrystalline or nanocrystalline solid.

For microstructures with a large number of defects in the total scattering volume the sum in Eq. (A2) can be replaced by an integral over the orientation of the defects. This is conveniently done in terms of a distribution function $s(\mathbf{q},\psi)$, defined so that

$$\sum_j S_{H,j}(\mathbf{q})=s(\mathbf{q},\psi)\,\delta\psi, \tag{A3}$$

the sum being over all defects with $\mathbf{h}(\mathbf{q})$ oriented in the interval $[\psi-\delta\psi/2,\psi+\delta\psi/2]$. By definition, the total S_H is the sum over all $S_{H,j}$, that is,

$$S_H(\mathbf{q})=\int_0^{2\pi} s(\mathbf{q},\psi)\,d\psi. \tag{A4}$$

We can therefore express the anisotropy of $s(\mathbf{q},\psi)$ by the Fourier series

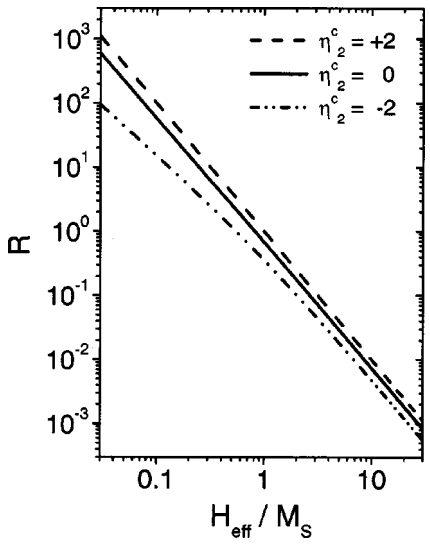

FIG. 14. The response function $\bar{R}$, Eq. (A10), versus the dimensionless parameter H_{eff}/M_S for different values of the texture coefficient η_2^c as indicated in the figure.

$$s(\mathbf{q},\psi)=\frac{1}{2\pi}S_H(\mathbf{q})\left(\frac{\eta_0^c}{2}+\sum_{w=1,2,3,\cdots}\eta_w^c(\mathbf{q})\cos w\psi + \eta_w^s(\mathbf{q})\sin w\psi\right), \tag{A5}$$

with $\eta_w^c(\mathbf{q})$ and $\eta_w^s(\mathbf{q})$ the Fourier cosine and sine coefficients, respectively, of the function $2\pi s(\mathbf{q},\psi)/S_H(\mathbf{q})$. For instance,

$$\eta_w^c(\mathbf{q})=2\int_{-\pi}^{\pi}\frac{s(\mathbf{q},\psi)}{S_H(\mathbf{q})}\cos w\psi\,d\psi \tag{A6}$$

and, in particular, $\eta_0^c(\mathbf{q})=2$. In terms of $s(\mathbf{q},\psi)$,

$$\frac{d\Sigma_M}{d\Omega}(\mathbf{q},H_i)=\int_0^{2\pi} s(\mathbf{q},\psi)R(\psi,\vartheta,q,H_i)\,d\psi. \tag{A7}$$

Substituting the Fourier series, Eq. (A5), for $s(\mathbf{q},\psi)$ in Eq. (A7), using Eq. (17) for R, and considering the symmetry of the products of trigonometric functions in the sum, it is readily seen that the value of the integral vanishes for all the terms except those involving the constant and $\cos 2\psi$; therefore

$$\frac{d\Sigma_M}{d\Omega}(\mathbf{q},H_i)=S_H(\mathbf{q})\frac{1}{2\pi}\int_0^{2\pi}(1+\eta_2^c(\mathbf{q})\cos 2\psi) \times R(\psi,\vartheta,q,H_i)\,d\psi. \tag{A8}$$

With R expressed by Eq. (17) this evaluates to

$$\frac{d\Sigma_M}{d\Omega}(\mathbf{q},H_i)=\frac{1}{2}S_H(\mathbf{q})\frac{M_S^2}{H_{\rm eff}^2}\frac{1}{\left(1+\frac{M_S}{H_{\rm eff}}\sin^2\vartheta\right)^2}\times\left[2-\left(1-2\frac{M_S}{H_{\rm eff}}\right)\sin^2\vartheta+\frac{M_S^2}{H_{\rm eff}^2}\sin^4\vartheta+\frac{\eta_2^c}{2}\left\{\left(1+2\frac{M_S}{H_{\rm eff}}\right)\sin^2\vartheta+\frac{M_S^2}{H_{\rm eff}^2}\sin^4\vartheta\right\}\right]. \tag{A9}$$

Assuming η_2^c to be a constant, independent of ϑ, we find for the azimuthal average response function, to be used with Eqs. (20) and (22),

$$\overline{R}(q,H_i)=\frac{1}{4}\frac{M_S^2}{H_{\rm eff}^2}\left[2+\frac{1}{\left(1+\frac{M_S}{H_{\rm eff}}\right)^{1/2}}+\frac{\eta_2^c}{2}\left(2-\frac{1}{\left(1+\frac{M_S}{H_{\rm eff}}\right)^{1/2}}\right)\right]. \tag{A10}$$

In the limit of $\eta_2^c(\mathbf{q})=0$, Eqs. (A9) and (A10) reduce to the results for the isotropic case, Eqs. (19) and (21).

It is readily seen that possible values for η_2^c are in the interval $[-2, 2]$: in the limiting case where the anisotropy field is entirely along $\mathbf{e}_y$ (in an experiment with a sheet sample with the incident beam along the normal of the sheet, this means that the anisotropy field acts exclusively in the plane of the sheet), $s(\mathbf{q},\psi)\propto\delta(\psi-\pi/2)+\delta(\psi+\pi/2)$, it is readily verified that $\eta_2^c=-2$. By analogous reasoning it is found that anisotropy exclusively along the sheet normal results in $\eta_2^c=+2$. Figure 14 displays the function $\overline{R}(q,H_i)$ versus the parameter $H_{\rm eff}/M_S$ for $\eta_2^c=0$ and for the extreme values $\eta_2^c=-2$ and $\eta_2^c=2$. It can be seen that for $H_{\rm eff}\gtrsim M_S$ different values of η_2^c lead to response functions $\overline{R}(q,H_i)$ that differ, approximately, by a constant factor, whereas the functional form of the dependency on the applied magnetic field remains almost unaffected. The anisotropy field-scattering functions computed from a given data set by analysis in terms of Eq. (22) will therefore depend on the choice of η_2^c only through a scaling factor, whereas the functional form of S_H will be little affected. Because real specimens will rarely exhibit the extreme anisotropy considered above, it will generally be a reasonable approximation to neglect the texture at the higher effective fields, and to use the result for isotropic microstructures, Eq. (21) in Sec. II C.

[1] N. C. Koon and B. N. Das, Appl. Phys. Lett. **39**, 840 (1981).
[2] J. J. Croat, IEEE Trans. Magn. **18**, 1442 (1982).
[3] G. Herzer, Mater. Sci. Eng., A **133**, 1 (1991).
[4] H. Kronmüller, in *Moderne Probleme der Metallphysik*, edited by A. Seeger (Springer, Berlin, 1966), Vol. 2, p. 24.
[5] C. Herring and C. Kittel, Phys. Rev. **81**, 869 (1951).
[6] S. Chikazumi, *Physics of Ferromagnetism*, 2nd ed. (Clarendon, Oxford, 1997).
[7] W. F. Brown, *Micromagnetics* (Wiley, New York, 1963).
[8] A. Aharoni, *Introduction to the Theory of Ferromagnetism* (Clarendon, Oxford, 1996).
[9] L. Landau and E. Lifshitz, Phys. Z. Sowjetunion **8**, 153 (1935).
[10] H. Hoffmann, J. Appl. Phys. **35**, 1790 (1964).
[11] K. J. Harte, J. Appl. Phys. **39**, 1503 (1968).
[12] E. M. Chudnovsky, W. M. Saslow, and R. A. Serota, Phys. Rev. B **33**, 251 (1986).
[13] M. Bachmann, R. Fischer and H. Kronmüller, in *Magnetic Anisotropy and Coercivity in Rare-Earth Transition Metal Alloys*, edited by L. Schultz and K.-H. Müller (Werkstoff-Informationsgesellschaft, Frankfurt, 1998), p. 217; R. Fischer and H. Kronmüller, J. Magn. Magn. Mater. **191**, 225 (1999).
[14] K. Suzuki and J. M. Cadogan, Phys. Rev. B **58**, 2730 (1998).
[15] J. R. Childress, C. L. Chien, J. J. Rhyne, and R. W. Erwin, J. Magn. Magn. Mater. **104–107**, 1585 (1992).
[16] C. Bellouard, I. Mirebeau, and M. Hennion, Phys. Rev. B **53**, 5570 (1996).
[17] U. Lembke, A. Hoell, R. Kranold, R. Müller, W. Schüpperl, G. Goerigk, G. Gilles, and A. Wiedenmann, J. Appl. Phys. **85**, 2279 (1999).
[18] W. Wagner, A. Wiedenmann, W. Petry, A. Geibel, and H. Gleiter, J. Mater. Res. **6**, 2305 (1991).
[19] J. Löffler, G. Kostorz, A. Wiedenmann, and W. Wagner, Physica B **241-3**, 603 (1998).
[20] G. Göltz, H. Kronmüller, A. Seeger, H. Scheuer, and W. Schmatz, Philos. Mag. A **54**, 213 (1986).
[21] J. Kohlbrecher, A. Wiedenmann, and H. Wollenberger, Z. Phys. B: Condens. Matter **104**, 1 (1997).
[22] J. Weissmüller, R. D. McMichael, A. Michels, and R. D. Shull, J. Res. Natl. Inst. Stand. Technol. **104**, 261 (1999), http://www.nist.gov/jres
[23] A. Michels, J. Weissmüller, A. Wiedenmann, and J. G. Barker, J. Appl. Phys. **87**, 5953 (2000).
[24] R. T. C. Choo, J. M. Toguri, A. M. El-Sherik, and U. Erb, J. Appl. Electrochem. **25**, 384 (1995).
[25] M. Azadegan, G. Palumbo, G. McMahon, T. Malis, G. A. Button, and U. Erb (unpublished).
[26] Equation (2) follows from Eq. (4.7) in Ref. 7 by conversion to SI units, using the somewhat more common notation (compare, e.g., Ref. 5 and Sec. 16.1 in Ref. 6) based on A instead of the exchange parameter $C=2A$. By comparison to Eqs. (3.36) and (3.50) in Ref. 7, it is readily seen that the explicit form of their term $\nabla^2\boldsymbol{\nu}$ is $\nabla^2\boldsymbol{\nu}=\{\nabla^2\nu_x,\nabla^2\nu_y,\nabla^2\nu_z\}$. A detailed derivation of Eq. (2) is also given in Sec. 8.3 of Ref. 8.
[27] A. Seeger and H. Kronmüller, J. Phys. Chem. Solids **12**, 298 (1960).
[28] W. Maass, U. Krey, and H. Hoffmann, J. Magn. Magn. Mater. **53**, 330 (1986).
[29] G. E. Bacon, *Neutron Diffraction*, 2nd ed. (Clarendon, Oxford, 1962).

[30] P. G. de Gennes, in *Magnetism*, edited by G. T. Rado and H. Suhl (Academic, New York, 1963), Vol. III, Sec. 3.
[31] S. W. Lovesey, *Theory of Neutron Scattering from Condensed Matter* (Clarendon, Oxford, 1984).
[32] W. G. Williams, *Polarized Neutrons* (Clarendon, Oxford, 1988).
[33] R. M. Moon, T. Riste, and W. C. Koehler, Phys. Rev. **181**, 920 (1969).
[34] O. Halpern and M. H. Johnson, Phys. Rev. **55**, 898 (1939).
[35] In order to comply with our previous notation in Ref. 22, we prefer the notation of Ref. 34 over that of Ref. 33, and display results in terms of **Q**, rather than its negative, $\mathbf{S}_{\perp}$.
[36] R. J. Elliot and R. D. Lowde, Proc. R. Soc. London, Ser. A **230**, 46 (1955).
[37] R. Stine, in *Modern Methods of Data Analysis*, edited by J. Fox and J. S. Long (Sage, London, 1990), pp. 325–373.
[38] R. D. Lowde and N. Umakantha, Phys. Rev. Lett. **4**, 452 (1960).
[39] A. I. Okorokov, V. V. Runov, B. P. Toperverg, A. D. Tret'yakov, E. I. Mal'tsev, I. M. Puzeĭ, and V. E. Mikhaĭlova, Pis'ma Zh. Eksp. Teor. Fiz. **43**, 390 (1986) [JETP Lett. **43**, 503 (1986)].
[40] M. W. Stringfellow, J. Phys. C **1**, 950 (1968).
[41] J. Beille, P. Pataud, and P. Radhakrishna, Solid State Commun. **18**, 1291 (1976).
[42] For magnon emission, where $k_1<k_0$ due to the neutron energy loss, the *scattering triangle*, which represents the vector equation for the balance of momentum, $\mathbf{k}_0=\mathbf{k}_1+\mathbf{q}$, can only be closed when the condition $k_1>k_0-q$ is satisfied. Similarly, for magnon absorption where $k_1>k_0$ it is required that $k_1<k_0+q$. By squaring these inequalities and by using the conservation of energy condition, $\hbar^2k_0^2/(2m)=\hbar^2k_1^2/(2m)\pm(Dq^2+g\mu_B\mu_0H)$, to eliminate k_1 one obtains

$$k_0^2-\frac{2m}{\hbar^2}(Dq^2+g\mu_B\mu_0H)>(k_0-q)^2$$

for emission and

$$k_0^2+\frac{2m}{\hbar^2}(Dq^2+g\mu_B\mu_0H)<(k_0+q)^2$$

for absorption. These expressions can be rearranged into

$$\frac{q}{2k_0}\left(\frac{2mD}{\hbar^2}\pm1\right)+\frac{mg\mu_B\mu_0H}{\hbar^2k_0q}<1$$

where + and − refer to magnon emission and absorption, respectively. This inequality restricts the range of q for which inelastic scattering is possible. The term ±1 in the brackets is ignored in the present work since it is negligible compared to the values of $2mD/\hbar^2$, which are 190 for Ni and 240 for Co. Simple algebra shows that the last inequality has no solutions in q when the magnetic field H exceeds the critical value H^* expressed by Eq. (23) in the main text, in other words for applied fields $H>H^*$ no inelastic scattering by absorption or emission of magnons is possible.
[43] A. Wiedenmann, J. Metast. Nanocryst. Mater. **2–6**, 315 (1999).
[44] A. M. El-Sherik and U. Erb, J. Mater. Sci. **30**, 5743 (1995).
[45] C. J. Glinka, J. G. Barker, B. Hammouda, S. Krueger, J. J. Moyer, and W. J. Orts, J. Appl. Crystallogr. **31**, 430 (1998).
[46] B. E. Warren, *X-ray Diffraction* (Dover, New York, 1990).
[47] H. P. Klug and L. E. Alexander, *X-Ray Diffraction Procedures for Polycrystalline and Amorphous Materials*, 2nd ed. (Wiley, New York, 1974), Chap. 9.
[48] J. Weissmüller, in *Nanomaterials: Synthesis, Properties, and Uses*, edited by A. S. Edelstein and R. C. Cammarata (Institute of Physics, Bristol, 1996), p. 219.
[49] C. E. Krill and R. Birringer, Philos. Mag. A **77**, 621 (1998).
[50] The grain size of the same sample was previously determined by analyzing the integral width of the Bragg reflections in terms of the method of Klug and Alexander (Ref. 47), ignoring broadening from twin boundaries. This yielded the erroneously low value of $d=18$ nm reported in Ref. 23.
[51] M. J. Aus, C. Cheung, B. Szpunar, and U. Erb, J. Mater. Sci. Lett. **17**, 1949 (1998).
[52] O. Halpern and T. Holstein, Phys. Rev. **59**, 960 (1941).
[53] W. H. Meiklejohn, J. Appl. Phys. **33**, 1328 (1962).
[54] J. Loeffler, J. P. Meier, B. Doudin, J.-P. Ansermet, and W. Wagner, Phys. Rev. B **57**, 2915 (1998).
[55] P. R. Bevington, *Data Reduction and Error Analysis for the Physical Sciences* (McGraw-Hill, New York, 1969), pp. 204–246.
[56] S. J. Pickart, H. A. Alperin, V. J. Minkiewicz, R. Nathans, G. Shirane, and O. Steinsvoll, Phys. Rev. **156**, 623 (1967).
[57] H. A. Mook, R. M. Nicklow, E. D. Thompson, and M. K. Wilkinson, J. Appl. Phys. **40**, 1450 (1969).
[58] J. W. Lynn and H. A. Mook, Phys. Rev. B **23**, 198 (1981).
[59] H. A. Alperin, O. Steinsvoll, G. Shirane, and R. Nathans, J. Appl. Phys. **37**, 1052 (1966).
[60] A. Guinier, *X-ray Diffraction in Crystals, Imperfect Crystals and Amorphous Bodies* (Freeman, San Francisco, 1963 and Dover, New York, 1994).
[61] G. Walter, R. Kranold, Th. Gerber, J. Baldrian, and M. Steinhart, J. Appl. Crystallogr. **18**, 205 (1985).
[62] R. Alben, J. J. Becker, and M. C. Chi, J. Appl. Phys. **49**, 1653 (1978).
[63] R. Schäfer, J. Magn. Magn. Mater. **215–216**, 652 (2000).